processes

MDPI

*Review*

# A Mini Review on Thin Film Superconductors

**David Sibanda, Sunday Temitope Oyinbo *, Tien-Chien Jen * and Ayotunde Idris Ibitoye**

Department of Mechanical Engineering Science, University of Johannesburg, Johannesburg 2006, South Africa; 218014683@student.uj.ac.za (D.S.); ibituns@gmail.com (A.I.I.)
* Correspondence: soyinbo@uj.ac.za (S.T.O.); tjen@uj.ac.za (T.-C.J.)

**Abstract:** Thin superconducting films have been a significant part of superconductivity research for more than six decades. They have had a significant impact on the existing consensus on the microscopic and macroscopic nature of the superconducting state. Thin-film superconductors have properties that are very different and superior to bulk material. Amongst the various classification criteria, thin-film superconductors can be classified into Fe based thin-film superconductors, layered titanium compound thin-film superconductors, intercalation compounds of layered and cage-like structures, and other thin-film superconductors that do not fall into these groups. There are various techniques of manufacturing thin films, which include atomic layer deposition (ALD), chemical vapour deposition (CVD), physical vapour deposition (PVD), molecular beam epitaxy (MBE), sputtering, electron beam evaporation, laser ablation, cathodic arc, and pulsed laser deposition (PLD). Thin film technology offers a lucrative scheme of creating engineered surfaces and opens a wide exploration of prospects to modify material properties for specific applications, such as those that depend on surfaces. This review paper reports on the different types and groups of superconductors, fabrication of thin-film superconductors by MBE, PLD, and ALD, their applications, and various challenges faced by superconductor technologies. Amongst all the thin film manufacturing techniques, more focus is put on the fabrication of thin film superconductors by atomic layer deposition because of the growing popularity the process has gained in the past decade.

**Keywords:** thin film superconductors; Meissner effect; atomic layer deposition; thin-film technology; pulsed laser deposition



**Citation:** Sibanda, D.; Oyinbo, S.T.; Jen, T.-C.; Ibitoye, A.I. A Mini Review on Thin Film Superconductors. *Processes* **2022**, *10*, 1184. https://doi.org/10.3390/pr10061184

Academic Editor: Prashant K Sarswat

Received: 31 January 2022
Accepted: 15 March 2022
Published: 14 June 2022



## 1. Introduction

Superconductors have a great potential to bring radical transformation of electrical power transmission, enabling high-capacity loss-less power distribution, and eliminating the Joule effect. Studies of superconductors over the recent years have aimed at finding a material that becomes superconductive above the liquid nitrogen boiling point. The study of superconductivity aims at perfecting and improving the current superconductors so that superconductivity can be achieved at a lesser cost. This will enable the generation of large magnetic fields for superconductivity magnets application in medicine and maglev trains at a lower cost. The purpose of this review is to discuss the various types of thin-film superconductors, their manufacturing techniques, their microstructure, and how superconductivity is brought about. The understanding of different types of superconductors and their nature of superconductivity will lay a foundation in the pursuit of high temperature superconductors for commercial applications.

At the superconductivity state, the electrical current flows from one point of the material to the next without any resistance at all (or with very little resistance in the magnitude of micro-ohms) [1–4]. No energy (sound, heat, light, etc.) is released from the material during superconduction [5]. This happens when the material's temperature is at or below its critical superconducting temperature ($T_c$), and when the magnetic field is below the material's critical magnetic field The superconductivity phenomenon was first reported in 1911 by Professor H.K Onnes and his associates C. Dorsman, G.J Flim, and G. Holst [1].

The team was investigating the behavior of materials near the absolute zero temperature. They discovered that mercury at 4.2 K had zero electrical resistance [6]. Various theories of superconductivity, such as the BCS (Bardeen, Cooper, and Schrieffer) theory [7], London theory [8,9], and the Ginzburg–Landau theory [10,11], have been proposed to explain the phenomenon of superconductivity. Several metals and alloys show electron-phonon coupling [12] driven superconductivity [13].

There are two types of superconductors (when classified according to their superconductivity property loss and retention when placed in a critical magnetic field); Type I and II superconductors. Type I superconductors (also called soft superconductors) [14] lose their superconductivity properties and become general conductors when put in a magnetic field that is higher than the critical magnetic field ($H_c$) of the material. They also conform entirely to the Meissner effect, which states that a superconductor at critical or below critical temperature expels all the magnetic field when placed in a magnetic field, provided that the field in question is less than the critical magnetic field of the material. Type I superconductors include basic conductive parts that are used in electrical cables and microchips of computers. Good examples are Zinc and Aluminium. Type I superconductors are good conductors at room temperature. They are normally used as general conductors at room temperature. Also identified as hard superconductors [15–17], Type II superconductors lose their superconductivity properties slowly but not simply when they are placed in a critical magnetic field. Their superconductivity loss begins on the less important magnetic field and then completely drops on the higher, more important critical magnetic field. The phase occurring amid the less critical magnetic field ($H_{c1}$) and the important higher critical magnetic field ($H_{c2}$) is termed an intermediate state or sometimes the vortex state [14]. Type II superconductors partially obey the Meissner effect. The reason they are called hard superconductors is that they lose their superconductivity slowly but not simply. Niobium Nitride (NbN) [18] and $BaBi_3$ are examples of these.

Conventional superconductors can either be Type I or Type II superconductors. They show superconductivity as defined by the BCS theory and its subsidiaries. Non-conventional superconductors do not conform to the BCS and Nikolay Bogolyubov theories. Superconductivity in conventional superconductors is due to electron–phonon-coupled superconducting electron pairs as defined by the BCS theory, but in unconventional superconductors, the Cooper pairs are bound by the exchange of some different type, for example, spin fluctuations in a superconductor with magnetic order either coexistent or nearby in the phase diagram [19,20]. Masahito et al. [21] define high temperature superconductors as those having a transition temperature ($T_c$) greater than 20 K. Strongly underdoped YBCO ($Y_1Ba_2Cu_3O_{7-\delta}$) is an example of high critical temperature superconductors (HTS). Other low and high critical temperatures will be discussed in this review. Throughout this review, high temperature superconductors will be regarded as those having a transition temperature greater than 20 K.

The Meissner effect explains that when a superconductive material is subjected to a magnetic field beneath the critical magnetic field magnitude of the material, during the change to the superconducting phase (meaning that the temperature will also be less than the $T_c$ the material), the magnetic field is ejected from the superconducting material and disappears in its interior [22,23], as illustrated by Figure 1.

If the magnetic field strength is increased to a value above the critical magnetic value, the superconductor becomes a normal conductor. The magnetic field exclusion is achieved by means of electric currents, which flow without any losses on the exterior around the superconductor and, by doing so, armour the superconductor interior from the magnetic field [22]. Figure 2 shows the flow of current in a superconductor without losses.

The Meissner effect shows that at the superconducting phase, the material exhibits perfect diamagnetism [24–26]. A diamagnetic material opposes an externally applied magnetic field. Figure 3 illustrates the limits of superconductivity. Even when the temperature is below $T_c$ of the material, when the material is exposed to a magnetic field exceeding the

material's critical magnetic field, the superconductive characteristics disappear, and the material becomes a normal conductor.

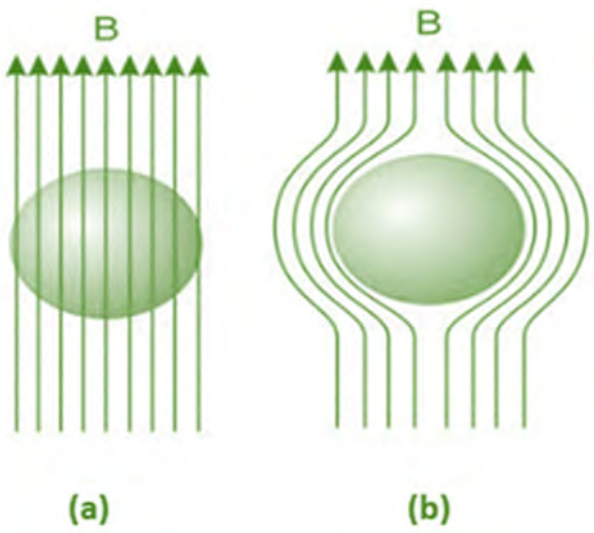


**Figure 1.** Behaviour of superconductive material experiencing a magnetic field (**a**) above and (**b**) less than the material's critical magnetic field. Magnetic flux can go through the material if the applied magnetic field is above the material's critical magnetic field as shown by (**a**), but will be expelled if the applied external magnetic field is less than the material's critical magnetic field as shown in (**b**).

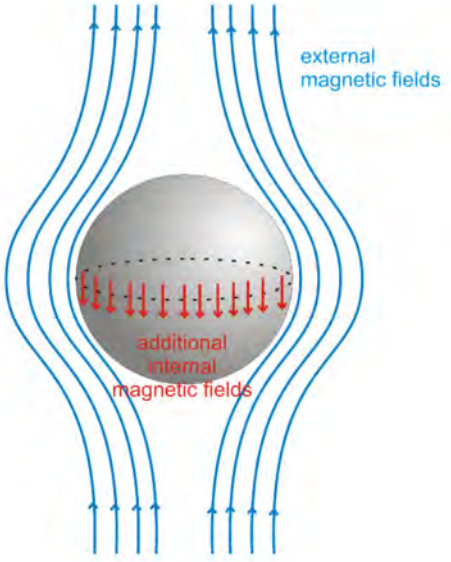


**Figure 2.** Flow of current in a superconductor. The flow of current on the material's surface shields the magnetic field and prevents it from reaching the interior of the material.

Gorter and Casimir [27] showed that the Meissner effect validity could be used to calculate the energy gap between the non-conducting and superconducting phases. They did this by considering the Gibbs free energy in the normal ($G_n$) and superconducting ($G_s$) phases. If the magnetic field is $H$, then:

$$G_s(T,H) = G_s(T,0) - \int_0^H M(H)\, dH, \tag{1}$$

where $M(H)$ is magnetisation. In perfect diamagnetism instances (e.g., in superconductors),

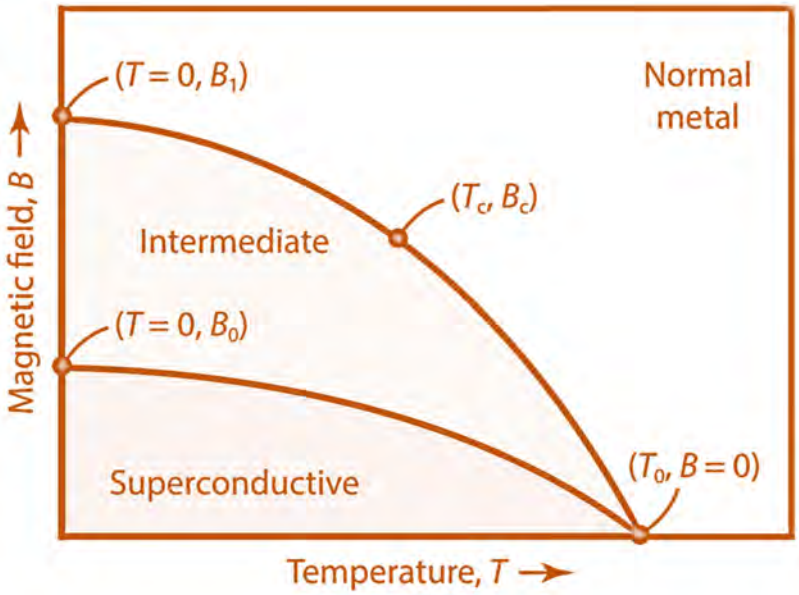


**Figure 3.** Limits of superconducting states. Superconductivity is only valid when the temperature and magnetic field density are below the critical temperature and critical magnetic field density of the material, respectively.

$$M(H) = -\frac{1}{4\pi}H. \tag{2}$$

The integral part of Equation (1) is the work done when the magnetic field is expelled. Factoring Equation (2) into (1), we get:

$$G_s(T,H) = G_s(T,0) + \frac{1}{8\pi}H^2. \tag{3}$$

Under equilibrium conditions at H is equal to $H_c$, $G_n$ $(T,H_c)$ is equal to $G_s$ $(T,H_c)$ and $G_n$ $(T,H_c)$ is equal to $G_n$ $(T,0)$. The energy gap between the normal and superconducting state is stated as:

$$G_n(T,0) - G_s(T,0) = \frac{1}{8\pi}H_c^2(T). \tag{4}$$

The shielding currents require a specific thickness layer close to the surface called magnetic penetration depth. This enables the magnetic field of the superconducting shielding current to neutralise the externally applied magnetic field. The shielding current density is defined by the equation,

$$J_s = \frac{H_c}{\lambda_m}, \tag{5}$$

where:

$J_s$—density of the shielding current;
$H_c$—critical magnetic field;
$\Lambda_m$—thickness of the layer.

Studies have shown that the properties of thin-film superconducting materials are far different and superior to those of the bulk material [28–32]. Thin films have improved electronic properties compared to the bulk material. The electronic properties are used to describe the behaviour and state of electrons in the material. These parameters include momentum and the electronic band structure, which defines the state of electrons in terms of their energy [33]. The electronic properties are strongly related to electric properties like dielectric response and electrical conductivity, and optical properties such as absorbance, damping constant, and refractive index. The atoms at the surface in a thin film have increased energy due to a smaller number of bonds with surrounding atoms. The more

energetic atoms at the grain boundaries of thin films makes them more chemically reactive than their bulk counterparts since they contain more exposed grains and grain boundaries [34,35]. Thin films have relatively lower costs of manufacturing, since they use much less material than their bulk counterparts. Since we have access to the deposition parameters, their properties can be tailored to suit our needs. The superconducting transition temperature of thin films changes with the film thickness and composition; hence it can affect the overall superconducting behaviour of the deposited material. The growth of thin films is an extremely active process where the kinetics that takes place during nucleation and the microscopic level growth are the crucial defining aspects for the resultant structure, morphology, and characteristics of the thin film. When one alters the deposition conditions or parameters, certain properties of the resulting films are also changed. Precise control of deposition temperature, thickness, and precursor concentration is therefore of paramount importance. In the nanometre scale range of film thickness, electron movements of the surface and boundary are confined and can lead to the formation of isolated electronic states called quantum well states [36]. When this happens, the overall electronic structure of the film changes due to the quantum size effect [37]. However, this does not happen each time the nanoscale is reached, but depends on the transport parameters of the used material. The physical properties of thin films vary significantly at small thicknesses. The variations of these properties of deposited films have been demonstrated in the electronic density of states [36,38], electron phono coupling [39,40], surface energy, and thermal stability [41,42].

Although the field of superconductors has received improved research interest among researchers, it still faces a number of challenges. Superconductors produce strong electromagnetic fields in the magnets, requiring heavy mechanical structures to counter the impact of Lorentz forces. The strong fields of the gantry magnets positioned close to the patient can result in more prolonged and powerful stray fields. The superconducting state is governed by a blend of three constraints: magnetic field ($H_c$), current density ($J_c$), and temperature ($T_c$), and temperature is the most difficult parameter to regulate because of the nearly 100% efficiency of the ultimate change of the magnetic and mechanical energy stored in the magnet to heat energy. The servicing of superconductive magnets might be difficult and require a devoted and highly skilled technical team responsible for the maintenance of the equipment Power applications of superconductivity lack a "compelling need" associated with either current or forthcoming energy societies since the present technologies perform acceptably. A room-temperature superconductor at atmospheric pressure is yet to be synthesised.

### *1.1. Theories of Superconductivity*

Three superconductivity theories will be discussed in this review. These are the London Theory, the Ginzburg–Landau Theory, and the BCS Theory.

#### 1.1.1. London Theory

This theory assumes that there is a consistency or stiffness in the superconducting state such that in the presence of the magnetic field the wave functions are not modified very much [8]. The kind of approach proposed by F London is called a classical approach. This theory models a superconductor as one in which charges are only influenced by the Lorentz force from an external field and not by any dissipative means [27]. This leads to the equation:

$$\frac{m}{ne^2}\frac{dJ}{dt} = E, \tag{6}$$

where:

$m$—mass of charge carrier;
$e$—charge;
$n$—density of the charge carriers;
$J$—current density.

Combining the parameters for convenience, a new constant can be found, as in the following equation

$$\Lambda = \frac{m}{ne^2}. \tag{7}$$

The London brothers started their theory by considering the effect of Equation (6), called the acceleration equation. Faraday's law implies that:

$$\nabla \times \left(\Lambda \frac{dJ}{dt}\right) = -\frac{dB}{dt}. \tag{8}$$

When displacement current is neglected, we have:

$$\nabla^2 (B - B_0) \frac{\Lambda}{\mu_0} = B - B_0. \tag{9}$$

The solutions of the above equation, which behave regularly inside the superconductor, decay exponentially to $B_{0,}$ as shown by the following equation:

$$\frac{B(x) - B_0}{B_{ext} - B_0} = e^{-\frac{x}{\lambda_L}}, \tag{10}$$

where $\lambda_L = \sqrt{\frac{m}{\mu_0 ne^2}}$.

$\lambda_L$ is called the London penetration depth. Typical values of $\lambda_L$ range between 50 nm and 500 nm.

In their theory of superconductivity, the London brothers assumed that there are two types of electrons; the normal electrons $n_n$ and the super electrons $n_s$. The concentration of normal electrons is large when $T > T_c$ and the concentration of super electrons is large when $T < T_c$. The concentration of super electrons is much greater than normal electrons in superconductors. When an electric field is applied, the following formula applies:

$$F = m\frac{dv}{dt} = eE, \tag{11}$$

where:

$v$—drift velocity of electrons;
$E$—electric field.

From the formula $I = Anev$, where $I$ is the current, $A$ is the area, $n$ is the concentration of electrons, $e$ is the electron charge and $v$ is the velocity; the current density is:

$$J = nev, \tag{12}$$

where $J$ is the current density. In superconductors, the concentration of super electrons is far much greater than those of normal electrons, hence the concentration of normal electrons can be neglected. The formula in superconductors becomes:

$$J_s = n_s ev, \tag{13}$$

where $j_s$ is the superconducting current density. On taking derivatives with respect to time, we have:

$$\frac{dJ_s}{dt} = n_s e \frac{dv}{dt}. \tag{14}$$

Substituting $dv/dt$ in Equation (14) by that in Equation (11), we get:

$$\frac{dJ_s}{dt} = \frac{n_s e^2 E}{m}. \tag{15}$$

Equation (15) is called London's first equation. From this equation, if the applied electric field is zero, then $J_s$ is a constant. This means that even when the electrical energy source is removed, the current will continue to flow.

By taking curl on both sides of Equation (15),

$$\nabla \times \frac{dJ_s}{dt} = \frac{n_s e^2}{m}(\nabla \times E),$$

$$\frac{d}{dt}(\nabla \times J_s) = \frac{n_s e^2}{m}(\nabla \times E). \tag{16}$$

Maxwell's third equation, which is written as

$$\nabla \times B = -\frac{\partial B}{\partial t}, \tag{17}$$

can be substituted into Equation (16) to get:

$$\frac{d}{dt}(\nabla \times J_s) = \frac{n_s e^2}{m}\left(-\frac{\partial B}{\partial t}\right). \tag{18}$$

When the left and right sides of the equation are integrated with respect to time, we get:

$$\nabla \times J_s = -\frac{n_s e^2 B}{m}. \tag{19}$$

Equation (19) is called London's second equation. The equation implies that at $B = 0$, $J_s$ is a constant.

Advantages of the London theory and equations:

i. It is the simplest theory of superconductivity;
ii. It captures the Meissner Effect and calculates the surface screening super currents;
iii. Receives only a single parameter, either $\lambda_L$ or n;
iv. Numerical complexity comparable to that of Maxwell;
v. Linear equations, so there's good convergence prospects.

Disadvantages of the London theory and equations:

i. Classical only, and has no quantum basis, therefore no treatment of secondary effects;
ii. Valid only in homogeneous materials;
iii. Cannot handle intermediate states, where different regions of the same material can be in different states of superconductivity, and formation of domains;
iv. It is a local theory and does not capture non local effect.

#### 1.1.2. Ginzburg–Landau Theory

This theory gives a quantitative description of superconductors near the transition point [5,11]. The theory states that there is a thermodynamic parameter that takes zero value in the symmetric phase occurring a high temperature and in the less symmetric it becomes zero continuously. The Free Energy density parameter ($r$), which is used to categorise superconductors, vanishes above critical temperature. The Ginzburg–Landau theory also successfully describes non-uniform field superconductors, effects of surface, quantisation of flux, and Type II superconductors.

This theory describes the superconductivity state with regards to a complex order parameter ψ(r), where;

Ψ(r) = 0, for $T > T_c$ and Ψ(r) $\neq$ 0, for $T < T_c$. this means the parameter is only valid in the superconducting state.

Ψ(r) approaches zero at $T = T_c$. the square of the modulus of this parameter gives the density of superconducting electrons.

Ψ(r) plays the same role as the wavefunction in the Schrodinger equation, describing all the condensed super electrons as a single charged particle. Ginzburg and Landau assumed that the force energy $F$ of a superconductor close to the superconducting transition can be expressed in terms of the complex order parameter ψ as

$$F_s = F_n + \alpha|\Psi|^2 + \frac{\beta}{2}|\Psi|^4 + \frac{(-i\hbar\nabla - qA)^2}{2m} + \frac{|B|^2}{2\mu_0}, \tag{20}$$

where:

$F_n$—free energy in the normal phase;
$\alpha$, $\beta$—phenomenological parameters;
$q$—2e for cooper pair;
$A$—electromagnetic vector potential;
$B$—the magnetic field strength;
$\mu_0$—magnetic permeability in a vacuum.

The first Ginzburg–Landau equation is derived by minimising the free energy with respect to the order parameter:

$$F_s = F_n + \alpha|\Psi|^2 + \frac{\beta}{2}|\Psi|^4 + \frac{|(-ih\nabla - qA)\psi|^2}{2m} + \frac{|B|^2}{2\mu_0}$$

$$\frac{\partial F_s}{\partial \psi} = 0 + 2\alpha\Psi + \frac{4B|\psi|^2\Psi}{2} + \frac{2}{2m}(-i\hbar\nabla - qA)^2\psi + 0$$

$$\alpha\psi + B|\psi|^2\psi + \frac{1}{2m}(-i\hbar\nabla - qA)^2\psi = 0. \tag{21}$$

When compared to the time independent Schrodinger equation, one notices that the first Ginzburg–Landau equation is similar to it, but is different from it due to the nonlinear term.

The time independent Schrodinger equation can be stated as follows:

$$-\frac{\hbar^2}{2m}\frac{\partial^2\psi}{\partial x^2} + V(x)\psi(x) = E\psi(x). \tag{22}$$

The second Ginzburg–Landau equation is obtained by minimising the free energy with respect to vector potential $A$

$$\frac{\partial F_s}{\partial A} = 0$$

$$J_s = \frac{2e}{m}\{\psi^*(-i\hbar\nabla - 2eA)\psi\}, \tag{23}$$

where:

$J_s$—is the superconducting electrical current density.

The second Ginzburg–Landau theory gives the superconducting current.

#### 1.1.3. BCS (Barden, Cooper, and Schrieffer) Theory

The BCS theory is based on the formation of a Cooper pairs. Electrical resistance is a result of collision of conducting electrons (free electrons) with the vibrating ions of the lattice in metals [7]. The force between the electrons is repulsive in the normal state, but it changes to be attractive in the superconducting state due to the formation of a Cooper pair. In their paper 'Theory of Superconductivity', Bardeen et al. [7] state that, 'the interaction between electrons resulting from virtual exchange of phonons is attractive when the energy difference between the electrons states involved is less than the phonon energy'. Two electrons that have opposite spin always combine with each other during pair formation [22]. One electron creates a positive charge fluctuation, which then attracts a second incoming electron behind it. This attraction continues creating a train of

electrons. In the superconducting state, the two electrons interact via a phonon or lattice distortion, forming a cooper pair. This means in a superconductor, electrons travel in a pair. Two electrons interact with each other through lattice vibrations in a process known as electron–lattice–electron interaction between the electrons via a phonon field [7]. A Cooper pair is a bond pair of electrons with opposite momenta and spin formed because of the interaction between the electrons in a phonon field. This electron pair do not transfer any energy to the lattice, meaning the substance does not have any electrical resistance giving infinite conductivity. The energy gap between these electrons is given by the equation:

$$\Delta = 2\hbar\omega_D exp\left[-\frac{2}{n(E_F)V}\right], \quad (24)$$

where:

$\Delta$—is the energy gap;
$\omega_D$—is the Deby frequency;
$n$—density of state of electrons at the fermi energy level $E_{F;}$
$V$—electron phonon coupling constant.

The energy of the bond pair is lower than that of separated normal electrons, which then favours the formation of Cooper pairs. The existence of this energy gap is supported experimentally by techniques such as:

i. The electronic specific heat of a superconductor at very low temperatures (close to 0 K);
ii. Ultrasonic absorption below $T_c$;
iii. Microwave/far infrared transmission in superconducting thin films and by tunnelling of electrons under I–V characteristics.

## 2. Thin Film Superconductors

Thin-film superconductors are frequently considered to be Type II superconductors even when they are from Type I materials because of the strong effect of the stray magnetic fields outside the superconductive sample [28]. Thin films can be defined as materials, where one dimension is highly constrained relative to the other two dimensions or a system whose properties are determined by the surface energy. Thin films consist of two main components: the microstructure and the surface morphology. The microstructure refers to the microscopic crystal structure of the thin film. Thin films fabrication has a virtually unlimited ability to synthesise materials with new or improved properties. This means new devices and applications can be realised. In this review, we grouped superconductors into four groups: Fe-based, layered titanium compounds, intercalation compounds with layered and cage-like structures, and other superconductors. The common methods of fabricating thin film superconductors are molecular beam epitaxy (MBE), pulsed laser deposition (PLD), atomic layer deposition (ALD), chemical vapour deposition (CVD), physical vapour deposition (PVD), electron beam evaporation, laser ablation, cathodic arc, sputtering, conventional solid-state reaction method, self-flux technique, high pressure high temperature synthesis technique, and arc melting technique.

### *2.1. Fe-Based Thin-Film Superconductors*

High-$T_c$ ($T_c$ > 20 K) superconductivity in Fe-based superconductors [21,43] was discovered in 2008 by Watanabe et al. [44]. Epitaxial iron-based thin-film superconductors [45] of very high quality are crucial in the manufacture of iron-based superconducting gadgets, like the Josephson junctions [46] and superconducting quantum interference devices (SQUIDs) [18]. They are also utilised in emerging iron-based superconductive coated conductors with high critical current density ($J_c$) under powerful magnetic fields. Thin films are also needed for academic purposes to realise the intrinsic characteristics of iron-based superconductors as substantial bulk solitary crystals are not easy to grow for some iron-based superconductors. There are various families/groups in which iron-based superconductors can be put into. In this paper, we identify these families as, *Ln*FeAs(O,F) (where

the *Ln* is the lanthanide element), also called the 1111 group, doped $AeFe_2As_2$ (where *Ae* is an alkaline-earth element) also the termed 122 group, Fe*Ch* (where *Ch* is a chalcogen) also termed the 11 group, and the FeSe mono-layer film, also called the 11-mono layer group. Molecular beam epitaxy and pulsed laser deposition are the most common Fe-based thin film fabrication and growth mechanisms. Several thin-film synthesis and applications articles [43,47–54] for iron-based thin-film superconductors have been published.

#### 2.1.1. LnFeAs(O,F) Family

The first high-$T_c$ iron-based superconductor to be discovered, with $T_c$ 26 K, is LaFeAs(O,F). It was discovered by Kamihara et al. [24,55]. They also discovered low-temperature iron-based superconductors, including LaFePO, whose $T_c$ is approximately 4K [56], LaNiPO whose $T_c$ is approximately 3 K [26] and LaNiAsO whose $T_c$ = 2.4 K [24]. These discoveries were made during the group's investigation of transparent p-type oxychalcogenide semiconductors like LaCuSO [26]. The group managed to increase $T_c$ to 55 K by replacement of a lanthanoid element (Ln) from Lanthanum to Neodymium [57]. The *Ln*FeAs(O,F) family is called the "1111" group. The following Figure 4 shows the LnFeAsO microstructure.

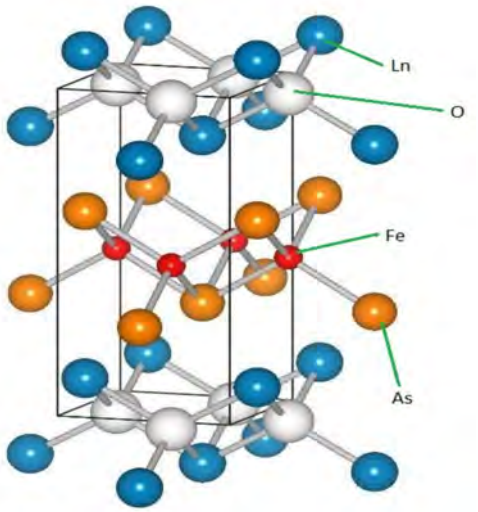


**Figure 4.** *Ln*FeAsO structure.

The growth of LaFeAs(O,F) thin-films was first attempted by Hiramatsu et al. [47]. Several processes such as reactive solid-phase epitaxy and simple pulsed laser deposition (PLD) growth were attempted to deposit the thin superconducting films of LaFeAs(O,F). Solid-phase epitaxy had been previously successful in growing LaZnOPn, but failed to produce satisfactory growth of LaFeAs(O,F). The breakthrough of getting the epitaxial films of LaFeAsO was brought by the simple pulsed laser deposition process (PLD). The Nagoya group employed molecular beam epitaxy (MBE) [58,59] and advanced the thin film growth of the 1111 compounds.

Backen et al. [60] reported on the synthesis of $LaFeAsO_{1-x}F_x$ superconducting film of polycrystalline by the ex-situ technique. They deposited the $LaFeAsO_{1-x}F_x$ films on MgO and $LaAlO_3$ substrates by a pulsed layer deposition method. Annealing was then done at elevated temperatures in an evacuated silica-glass tube to obtain the superconducting thin films. The thin film transitioned into a superconducting state at approximately 11 K. The superconducting thin films showing a zero resistivity around the critical temperature of bulk samples were positively synthesised by reviewing the annealing state [61].

Naito and Ueda et al. [62] reported on the SmFeAsO (Sm1111) thin film on $CaF_2$ substrate synthesised by molecular beam epitaxy. The film transitioned into a superconducting state at around 56 K. This was somewhat higher than $T_c$ of SmFeAs(O,F) bulk samples [59,62]. $CaF_2$ was first used by Tsukada et al. [63] as a substrate in the deposition

of $FeSe_{1-x}Te_x$. $CaF_2$ is effective in the manufacture of other iron-based superconductors, as evidenced by the enhancement of $T_c$ in Sm1111 film [62].

Haindl et al. [64] grew superconductive Sm1111 films on $CaF_2$ substrates using pulsed layer deposition. They noted that SmFeAs(O,F) films synthesised on $BaFe_2As_2$-buffered MgO substrates by employing the $SmFeAsO_{0.9}F_{0.1}$ polycrystalline target had virtually identical lattice parameters with those of SmFeAsO bulk samples. They, however, exhibited a glitch, alleged to be a result of structural transition [65], near a temperature of 150 K and no superconductivity in the temperature dependence of resistivity. These findings showed the insufficiency of the F content in this film. The Sm1111 film on $CaF_2$ substrate fabricated from the identical target transitioned into a superconducting state at 40 K.

#### 2.1.2. Doped $AeFe_2As_2$ family

In the second group (doped *Ae*$Fe_2As_2$ or (Ae,K)$Fe_2As_2$), usually termed "122" compounds [66,67] the one with the highest $T_c$ of ~38 K is $Ba_{0.65}K_{0.35}Fe_2As_2$. The compounds in this group have the crystal structure of $ThCr_2Si_2$ type. There is an alternating stacking of tetrahedron $Fe_2Pn_2$ layers and plain Ae layers in this family of compounds [21]. Pn is the pnictogen atom, it can either be As or Sb. Figure 5 shows the *Ae*$Fe_2As_2$ structure.

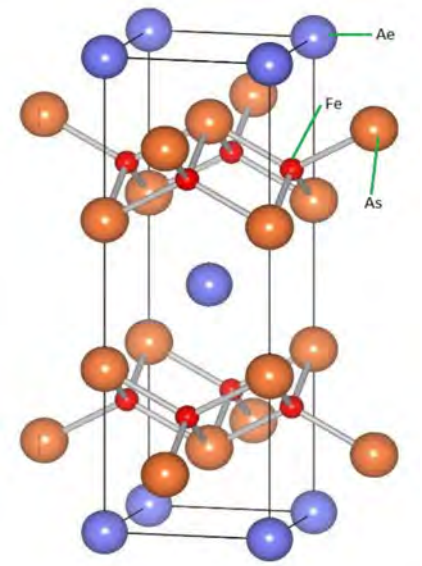


**Figure 5.** *Ae*$Fe_2As_2$ structure. The alternating stack of tetrahedron $Fe_2Pn_2$ layers and plain Ae layers can be seen in this structure.

Thin films of (Ae,K)$Fe_2As_2$ can be synthesised by using FeAs self-flux or Sn flux under ambient pressure. (Ae,K)$Fe_2As_2$ films growth is more difficult than LnFeAs(O,F) films. A group from Sungkyunkwan University synthesised superconductive (Ba,K)$Fe_2As_2$ films by a post-annealing method [68,69]. The TAT (Tokyo University of Agriculture and Technology) group synthesised thin films of (Ba,K)$Fe_2As_2$ and (Sr,K)$Fe_2As_2$ by molecular beam epitaxy [70–73]. Potassium is very volatile; therefore, it is not included in films grown at Ts > 400 °C. The TAT group worked on finding new superconductors and improving the $T_c$ of Fe-based superconductors. Potassium-containing 122 films synthesis is performed at Ts $\leq$ 400 °C. The Fe-based superconductor $Ba_{1-x}K_xFe_2As_2$ is used as a key material for high magnetic field applications such as superconducting wires and bulk permanent magnets.

#### 2.1.3. FeCh and FeSe Mono-Layer Film Family

In the family of Fe*Ch*, also called the 11 compounds, divalent chalcogen ions surround the divalent Fe ions tetrahedrally. Fe*Ch* structure is a sequential stacking of neutral tetrahedron $Fe_2Ch_2$ layer by van der Waals interaction. The Wu group [74] discovered the superconductivity in FeSe (whose $T_c$ is approximately 8.5 K) [55,75] and $FeSe_{0.5}Te_{0.5}$ (whose

$T_c$ is approximately 14 K) [75] after the report on the unearthing of superconductivity in LaFeAs(O,F) by Hosono and his colleagues [53]. The critical temperature of FeSe can be increased significantly when hydrostatic pressure is applied. It reaches 37 K at around 10 GPa [76,77]. Figure 6 shows the structure of FeSe.

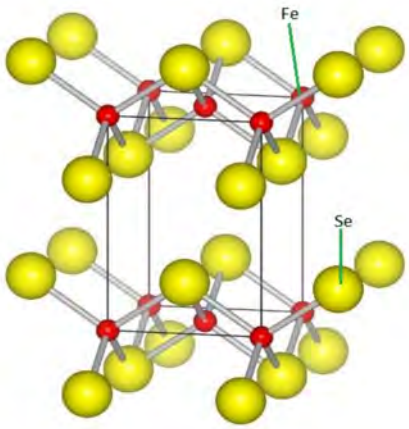


**Figure 6.** FeSe structure. Reddish brown balls are Fe atoms, while yellowish balls represent Se atoms.

The synthesis of group "11" iron-based thin films has been slow due to their toxicity [21]. $FeSe_{1-x}Te_x$ thin films growth was first realised by Wu et al. [74] by a pulsed laser deposition technique. Bellingeri et al. [78] reported that $T_c$ in $FeSe_{0.5}Te_{0.5}$ thin films could be increased up to 21 K from around 14 K by varying thickness. Figure 7 shows the thickness dependence of $T_c$ that they reported.

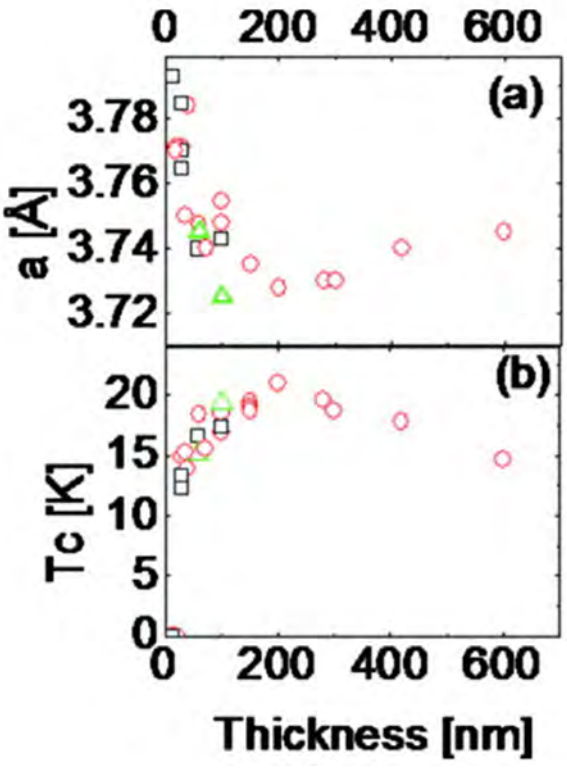


**Figure 7.** $T_c$ thickness dependence of $FeSe_{0.5}Te_{0.5}$ films. In (**a**) the thickness is plotted vs. lattice constant a [Å] while in (**b**) the thickness is plotted vs. $T_c$ [K]. Structural analyses showed that the $c_{film}$ (=5.84–5.89 Å) is less than the bulk values ($c_{bulk}$ = 5.995 Å) though independent of the film thickness.

Hanzawa and his colleagues [79] synthesised FeSe films, which were 100 Å thick on $SrTiO_3$ by molecular beam epitaxy. The highest $T_c$ obtained was 35 K. Lei et al. [80] conducted comparable experiments employing the flux method to grow FeSe single crystals. Table 1 summarises some of the transition temperatures of superconduction of the FeSe and Fe(Se,Te) thin films synthesised by molecular beam epitaxy and pulsed layer deposition.

**Table 1.** Transition temperatures of FeSe and Fe(Se,Te) thin-film superconductors manufactured by molecular beam epitaxy and pulsed laser deposition techniques.

| Materials | Substrate | Method | Transition Temp (K) | References |
|---|---|---|---|---|
| FeSe | r-cut $Al_2O_3$ | MBE | $T_{c(onset)}$ = 13 K | [70] |
| | $CaF_2$ | PLD | $T_{c(onset)}$= 12.4 K, $T_{c(end)}$ = 11.9 K | [81] |
| mono-layer FeSe | $SrTiO_3$ | MBE | $T_c$ = 42 K | [82] |
| | $SrTiO_3$ | | $T_c$ = 65 ± 5 K | [83] |
| | Nb-doped $SrTiO_3$ | | $T_c$ = 109 K | [84] |
| $FeSe_{1-x}Te_x$ x = 0.0~1.0 | MgO | PLD | $Tc_{(onset)}$~14 K, $T_{c(end)}$ ~ 12 K at x = 0.5 | [74] |
| $FeSe_{0.5}Te_{0.5}$ | $SrTiO_3$ | PLD | $T_c$ = 17 K | [85] |
| $FeSe_{0.5}Te_{0.5}$ | $LaAlO_3$ | PLD | $T_c$ = 21 K | [85] |
| $FeSe_{0.5}Te_{0.5}$ | $CaF_2$ | PLD | $T_{c(onset)}$ = 16.3 K, $T_{c(end)}$ = 15.3 K | [63] |
| $FeSe_{0.8}Te_{0.2}$ | | PLD | $T_c$ = 23 K | [86] |
| $FeSe_{0.72}Te_{0.18}$ | | PLD | $T_{c(onset)}$ = 22 K, $T_{c(end)}$ = 20.5 K | [87] |
| $FeSe_{0.5}Te_{0.5}$ | $SrF_2$ | PLD | $T_c$ = 15.7 K | [88] |
| $FeSe_{0.5}Te_{0.5}$ | $BaF_2$ | PLD | $T_c$ = 12.8 K | |
| $FeSe_{0.5}Te_{0.5}$ | Fe-buffered MgO | PLD | $T_c$ = 17.7 K | [21,89] |
| $FeSe_{0.5}Te_{0.5}$ | $CeO_2$-buffered YSZ, RABiTS | PLD | $T_{c(onset)}$ = 20 K, $T_{c(end)}$ = 18 K | [90] |
| $FeSe_{0.5}Te_{0.5}$ | $CeO_2$-buffered $SrTiO_3$ | PLD | $T_{c(onset)}$ = 18.5 K, $T_{c(end)}$ = 18 K | [91] |
| $FeSe_{0.5}Te_{0.5}$ | $FeSe_{1-x}Te_x$-buffered MgO | PLD | $T_{c(onset)} \geq$ 17 K | [92] |

Wang and his group [82] detected large energy gaps that possessed superconducting properties using scanning tunnelling spectroscopy (STS) at low temperatures in mono-layer FeSe thin films on $TiO_2$-terminated STO (perovskite $SrTiO_3$) grown by molecular beam epitaxy. The U-shaped gap was found to have a magnitude of 40.2 meV at 4.2 K.

### *2.2. Layered Titanium Compounds*

Layered titanium oxypnictides parent compounds are metallic without carrier doping, unlike cuprate superconductors [93–95]. Hosono et al. [48,49] prepared the $BaTi_2Sb_2O$ compound in 2012 and detected a bulk transition into superconductivity at a temperature of 1 K [96]. Doan and his group [97] autonomously presented an improved $T_c$ of 5.5K in $BaTi_2Sb_2O$ when it was doped with Na. $BaTi_2Sb_2O$ was prepared via the solid-state reaction technique using very pure BaO, Ti, and Sb according to their stoichiometric ratios [96]. This involved wrapping the specimen in a tantalum foil, sealing in a quartz tube and heating for a period of 40 h at an elevated temperature of 1000 °C. The sample was then cooled at a rate of 50 °C per hour up until room temperature was reached. The resulting compound

had a tetragonal structure. X-ray diffraction and neutron diffraction data was used to determine the crystal structure of $BaTi_2Sb_2O$. It showed that the crystal structure is the same as that of $BaTi_2As_2O$ [98]. Figure 8 shows the various crystal structures of layered titanium compounds. The $T_c$ of $BaTi_2Sb_2O$ was found to be 1.36 K. Figure 9 shows the synchrotron X-ray diffraction refinement results for $BaTi_2Sb_2O$ and $BaTi_2Bi_2O$ with the P4/mmm space group.

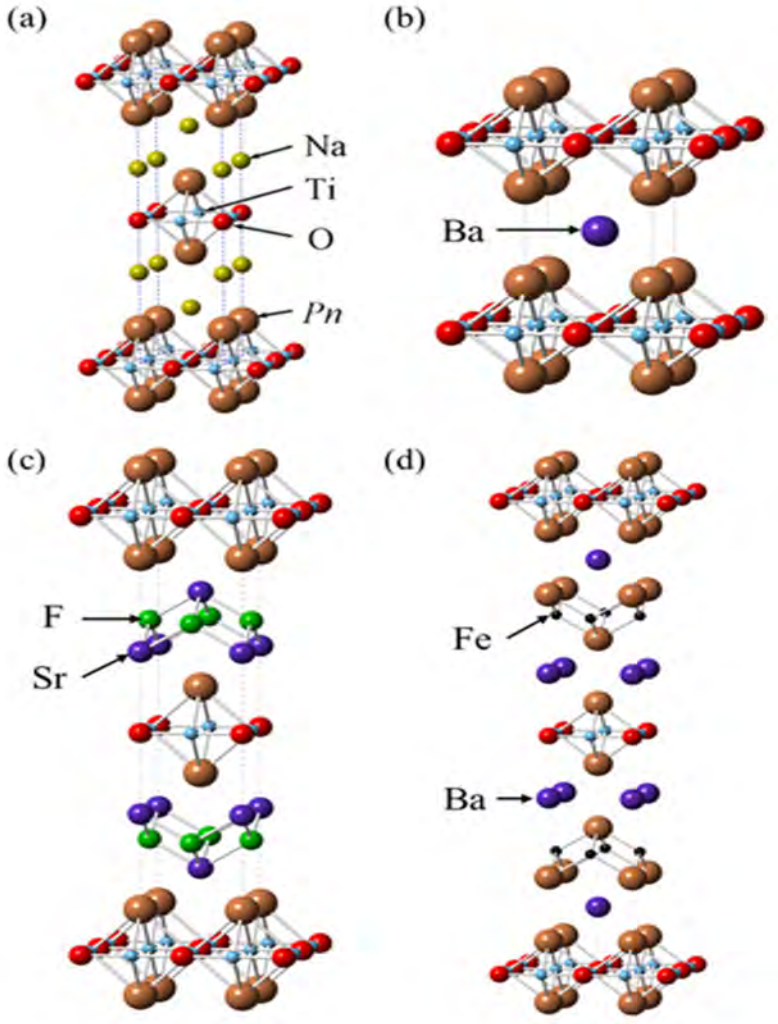


**Figure 8.** Crystal structures of different layered titanium compounds (**a**) $Na_2Ti_2Pn_2O$, (**b**) $BaTi_2Pn_2O$, (**c**) $(SrF)_2Ti_2Pn_2O$, and (**d**) $(Ba_2Fe_2As_2)Ti_2As_2O$ [54]. Pn is either Sb or As.

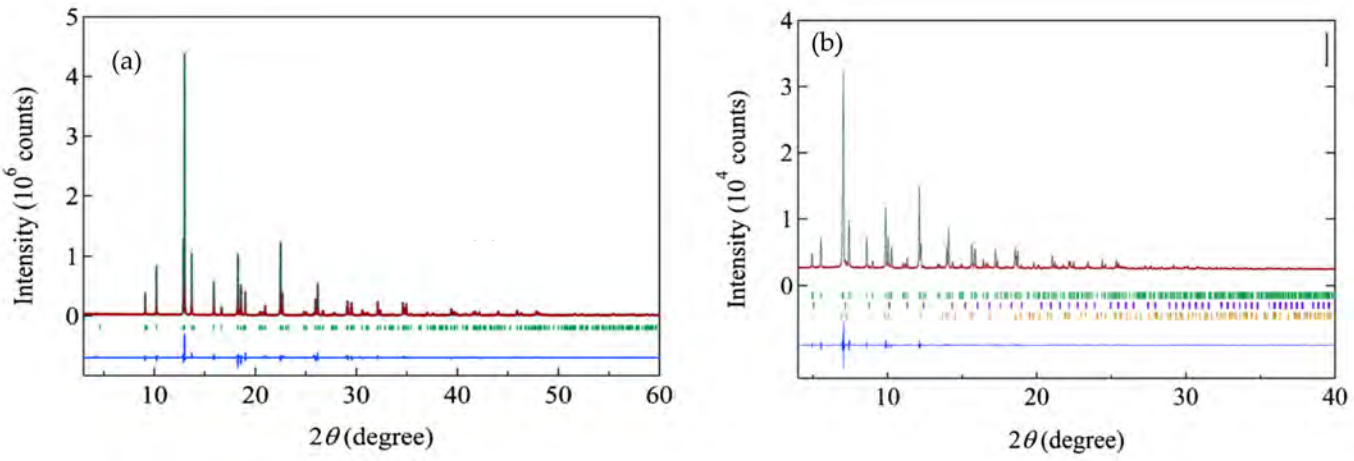


**Figure 9.** Refined synchrotron x-ray patterns of (**a**) $BaTi_2Sb_2O$ and (**b**) $BaTi_2Bi_2O$. The Bragg reflection positions are shown by the green ticks [54].

The Ti pnictide oxides $BaTi_2Pn_2O$ (where Pn is Sb or Bi) contain layers of superconductive $Ti_2Pn_2O$ and Barium blocking layers [98]. Several titanium pnictide oxides have been produced. These include $Na_2Ti_2Pn_2O$ (where Pn is As or Sb), $(SrF)_2Ti_2Pn_2O$ (where Pn is As, Sb, or Bi), and $BaTi_2Pn_2O$ (where Pn is As, Sb, or Bi). Amongst these compounds, only $BaTi_2Pn_2O$ (where Pn is Sb or Bi) shows superconductive characteristics [96,97,99–102]. $BaTi_2Sb_2O$ and $BaTi_2Bi_2O$ were manufactured using the conventional solid-state reaction [96,98]. $BaTi_2Bi_2O$ is unstable in air and some solvents, as it easily decomposes when exposed to air forming Bi-based phases such as $BaBi_3$ and Bi. Figure 10 shows the resistivity and magnetic susceptibility of $BaTi_2As_2O$. The electronic structure of a compound is vital in understanding its superconductivity. The $BaTi_2Sb_2O$ electronic structure as reported by Singh [103] from first principles calculation showed that three d orbitals $d_{xy}$, $d_{x^2-y^2}$, and $d_{z^2}$ have a substantial contribution at the Fermi level. This indicates that $BaTi_2Sb_2O$ has a multiband nature. The oxygen 2p and Antimony (Sb) 5p are filled, while the Antimony 5p are hybridised with Titanium 3d. No Ba-derived occupied valence bands are present. The formal valence shown by the results is $Ba^{2+}Ti^{3+}Sb^{3-}O^{2-}$. The one 3d electron of Ti is responsible for the transport and magnetic characteristics of the composite [95]. In the $BaTi_2Bi_2O$ electronic structure, as reported by Suetin and Ivanovskii [104], the three d orbitals have a substantial contribution at the Fermi level as is the case with $BaTi_2Sb_2O$.

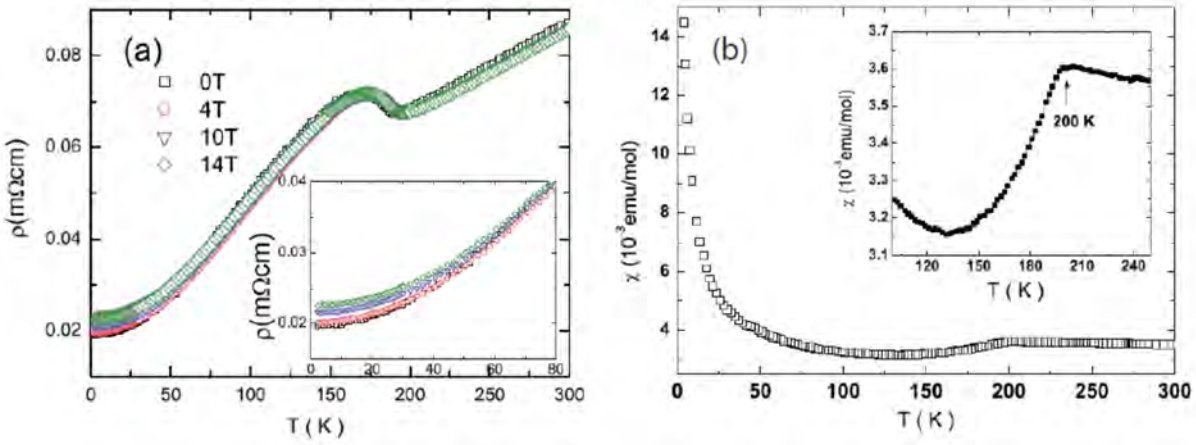


**Figure 10.** (**a**) The resistivity curve and (**b**) magnetic characteristics of $BaTi_2As_2O$. The low-temperature enlarged scale magnetic field effect is shown by the inset in (**a**) [54].

### *2.3. Intercalation Compounds with Layered and Cage-like Structures*

Examples of high-temperature superconductors with layered or cage-like structures are cuprates [105,106], iron pnictides [24,44,107], $MgB_2$ [51,108,109] and alkali metal-doped fullerides [54]. Their intercalated structures are made of charged (doped) layers attached to charge basins in the interlayer/cage-like space. There are two sub-families of layered polymorphs in metal nitride halides: the α-form and β-forms with stoichiometric formula MNX (where M is Ti, Zr, or Hf, N is Nitrogen and X is Cl, Br, or I). The α-form is an orthogonally MN layered network divided by halogen atoms, while the β-form contains dual honeycomb-like MN layers squeezed in between compact halogen layers [110,111]. MNX compounds are prepared by reacting the metal or metal hydride with ammonium halides at elevated temperatures [112]. The chemical reaction is:

$$M\ (or\ MH_2) + NH_4X\ \rightarrow MNX + 2\ (or\ 3)H_2.$$

MNX compound was then ferried in a quartz glass tube with a little amount of $NH_4X$ using a furnace whose temperature was between 750 and 850 °C. The resulting compounds were of α-form. The β-form was obtained by subjecting the α-form to a pressure of between 3 and 5 GPa at a temperature of around 800 °C. These superconductors have no magnetic ions, hence a magnetic pairing mechanism is not considered, but the possible candidates for the pairing mechanism have been assumed to be charge and spin fluctuations [113–115]. Figure 11 shows the α- and β-form structures of the metal nitride halides.

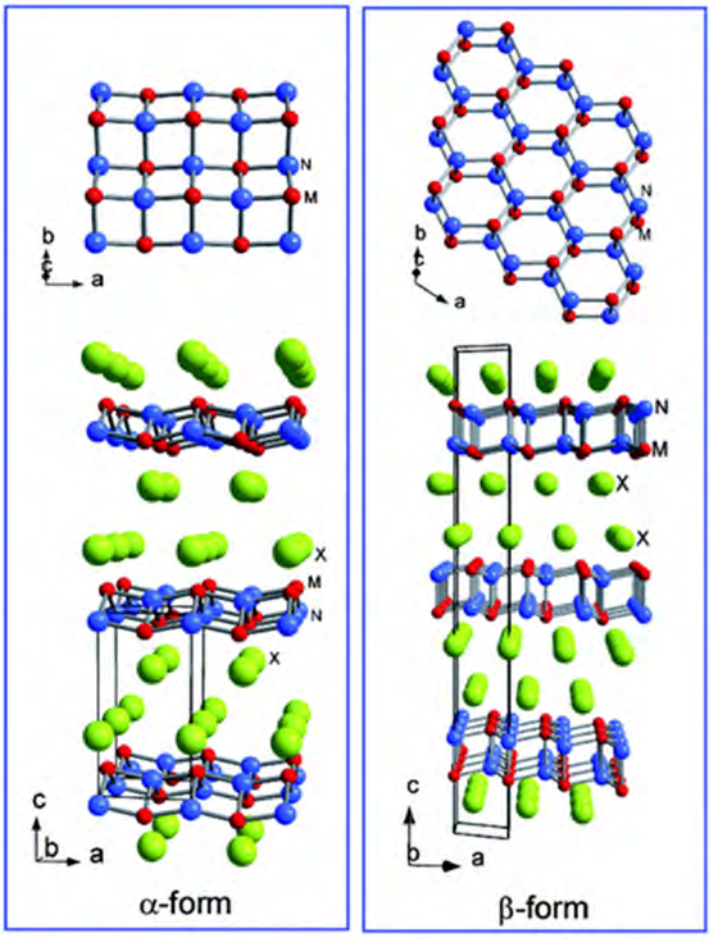


**Figure 11.** Crystal structures of the α-form and the β-form of (where M is Ti, Zr, or Hf and X is Cl, Br, or I). The red atoms represent the metal (M) atoms; the blue are the Nitrogen atoms, and the green are halogen atoms (X).

When β-HfNCl is doped by intercalation of alkali metals, a high-temperature superconductor ($T_c$ > 20 K) is obtained [54]. Yamanaka et al. [116] detected the highest $T_c$ value of 25.5 K in the lithium and tetrahydrofuran (THF) co-intercalated superconductor $Li_{0.48}(THF)_yHfNCl$. Earlier, Yamanaka et al. [117] found Zr homologue $Li_xZrNCl$ to exhibit superconductive characteristics at $T_c$ of approximately 14K. α-TiNCl required electron doping with alkali metals and organic bases like pyridine and alkylene diamines to be transformed into a superconductor [54]. Magnetic susceptibility was conducted on the Lithium intercalated sample, $Li_{0.56}HfNBr$, from the chemical reaction with *n*-BuLi in hexane. The following Figure 12 shows the temperature dependence of the magnetic susceptibility of $Li_{0.56}HfNBr$.

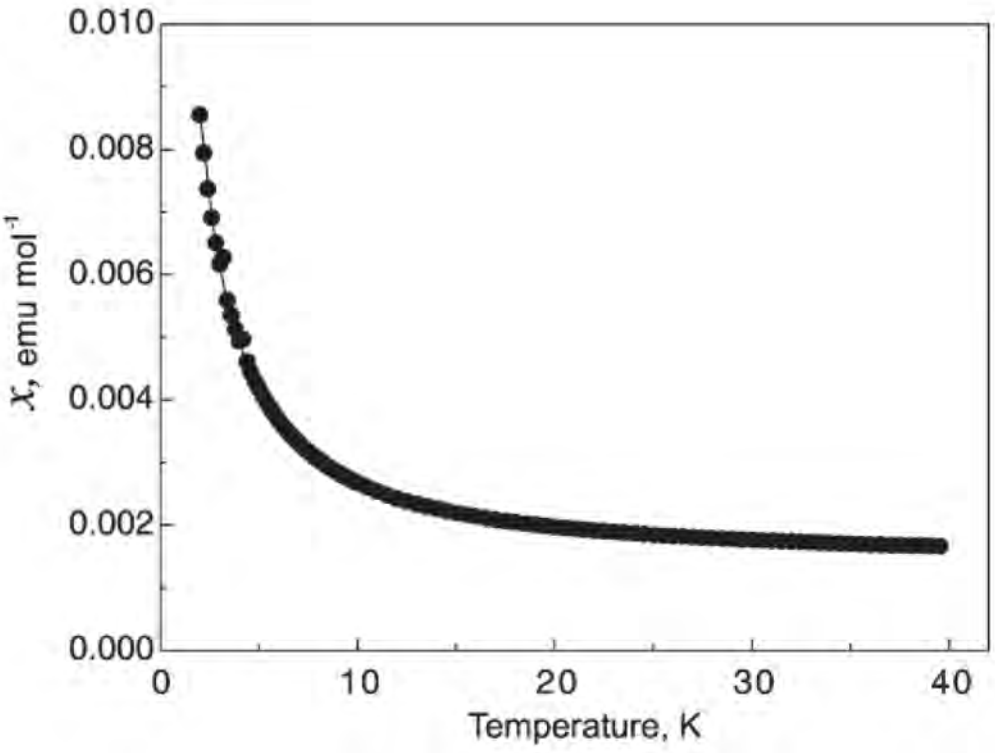


**Figure 12.** Temperature dependence of the magnetic susceptibility of $Li_{0.56}HfNBr$. $\chi = C/(T-\theta) + \chi_0$. C is the curie constant and has the value of 0.0145(1) emu K $mol^{-1}$, θ = 0.04(2) K and $\chi_0$ = 0.00126(1) emu $mol^{-1}$.

There are also silicon clathrates and related compounds that have cage-like structures. High pressure and high temperature (HPHT) conditions can be used to prepare the Ba-containing silicon clathrate compound $Ba_8Si_{46}$. The compound displays superconductivity at $T_c$ = 8.0 K [110]. HPHT application is favourable for synthesising binary phases that are rich in Si such as $LaSi_5$, $LaSi_{10}$, $BaSi_6$, $Ba_{24}Si_{100}$, $Ba_8Si_{46}$, $NaSi_6$, $Na_8Si_{46}$, and $Na_xSi_{136}$ [54,110,118–120]. Tanaka et al. [121] synthesised $Ca_2Al_3Si_4$ using the HPHT method. The compound showed superconductive transition at $T_c$ = 6.4 K.

### *2.4. Other Superconductors*

In this group, we discuss the superconducting compounds that fall outside the previous categories already mentioned. These compounds fall into the low-temperature and high-temperature superconductors.

$AM_2X_2$-type (where M is not Fe) superconductors are an example of 122-type superconductors. Some non-Fe 122-superconductors have the $ThCr_2Si_2$-type structure and include compounds such as $SrNi_2P_2$ [122], $BaNi_2P_2$ [107], $BaRh_2P_2$, $BaIr_2P_2$ [123], $LaRu_2P_2$ [124], $LiCu_2P_2$ [125], $SrNi_2As_2$ [126], and $BaNi_2As_2$ [127]. An example of 122-type antimonides

and associated compounds is $SrPt_2Sb_2$ [128]. Its measurements of electrical resistivity, magnetisation, and specific heat indicated a transition into superconductivity at $T_c$ = 2.1 K. The compound was manufactured by Hosono et al. [54] in two steps; arc melting and remelting of the specimen starting from Sr, Pt, and Sb. The superconductor is of Type II and has a lower critical field ($H_{c1}$) and upper critical field ($H_{c2}$) of 6 Oe and 1 kOe, respectively, at a temperature of 1.8 K [54].

Cobalt-based superconductor $LaCo_2B_2$ [129] was synthesised using the arc-melting technique for Lanthanum, Cobalt, Boron, Yttrium, and Iron mixtures. It was found to be superconductive after constituent cation isovalent or aliovalent substitution [54]. Density Functional Theory (DFT) was used to investigate the electronic structure of $LaCo_2B_2$. From these calculations, it was confirmed that La ions take +3 state. It was also confirmed that the strong covalent CoB layer is responsible for metallic conduction. Pauli paramagnetic state results due to the suppression of the spin moment of the Co ion by this strong covalency [54]. Figure 13 below shows the calculated Density of State (DOS) of the $LaCo_2B_2$ compound.

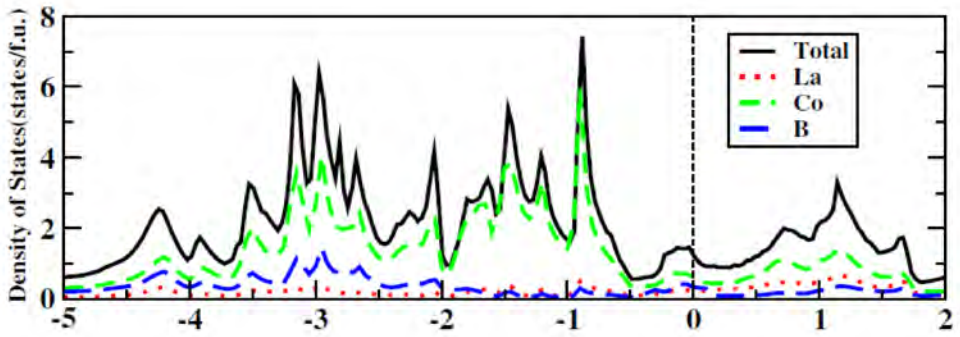


**Figure 13.** Calculated density of state (DOS) of $LaCo_2B_2$.

$BaNi_2As_2$ has a tetragonal $ThCr_2Si_2$ type crystal structure at room temperature [127,130,131] and undertakes a transition of its structure at approximately 130 K to a triclinic structure where alternate Nickel-Nickel bonds are created in the Nickel plane. This new phase shows conventional BCS type superconductive characteristics below 0.7 K [127,131–133]. The BCS type superconductivity is based on the formation of Cooper pairs. The electron-electron interaction that results from virtual exchange of phonons is non-repulsive when the energy difference between the electrons states concerned is below the phonon energy. During pair formation, two electrons with opposite spin always combine with each other [22]. One electron creates a positive charge fluctuation, which then attracts a second incoming electron behind it. This attraction continues creating a train of electrons. In the superconducting state, the two electrons interact via a phonon or lattice distortion forming a cooper pair. $BaNi_2As_2$ superconductivity can be enhanced through phosphorus doping, the transition temperature, which is lower than 0.7 K for the triclinic phase with $x$ less than 0.07, is increased to 3.33 K in the tetragonal phase with $x$ = 0.077. Hosono et al. [54] grew single crystals of $BaNi_2(As_{1-x}P_x)_2$ by a self-flux method using mixtures of Ba, NiAs, Ni, and P. Figure 14 shows the temperature dependence of electrical resistivity parallel to the *ab* plane. *ρab* was normalised by the value at 300 K for $BaNi_2(As_{1-x}P_x)_2$. Phosphorus doping suppresses the triclinic phase, leading to the improvement of superconductivity. Figure 15 shows the $BaNi_2(As_{1-x}P_x)_2$ system phase diagram.

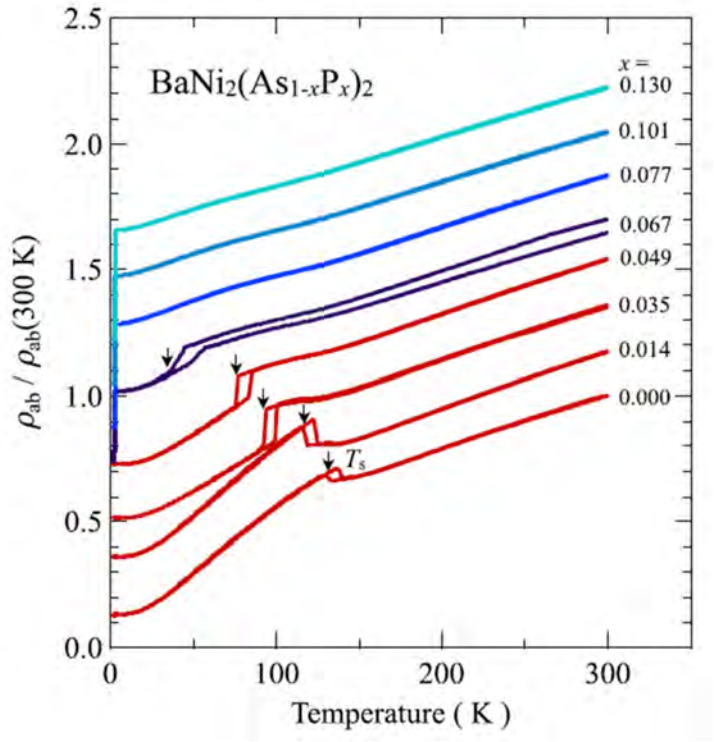


**Figure 14.** Temperature dependence of electrical resistivity parallel to the *ab* plane for $BaNi_2(As_{1-x}P_x)_2$ crystal. The resistivity arnomally shown by thermal hysterisis in the figure shows tetragonal to triclinic transition [134].

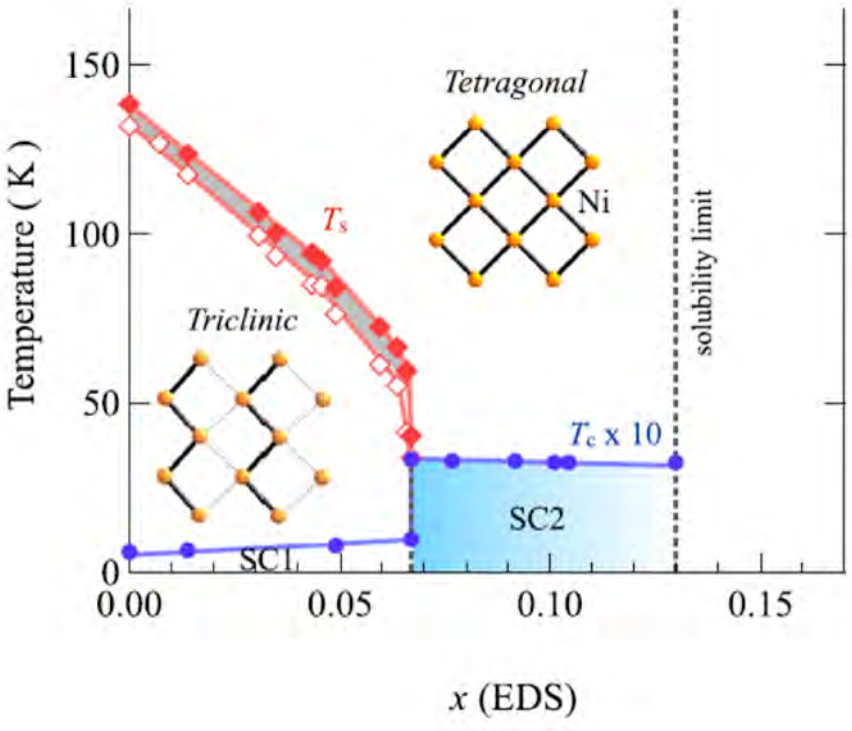


**Figure 15.** $BaNi_2(As_{1-x}P_x)_2$ system electronic phase diagram [134]. SC1 and SC2 shows the phases of superconduction. Tetragonal-to-triclinic structural transition temperatures (Ts) upon cooling and heating are shown by open and closed diamonds, respectively. Ni planes in the triclinic and tetragonal phase are shown by the inserts.

Transition metal dichalcogenides $MX_2$ have two families; $CdI_2$-type telluride family and the pyrite ($FeS_2$)-type chalcogenide family [54]. Self-flux technique was used to grow crystals of $IrTe_2$ [135]. This involved mixing powders of Ir and Te at a ratio of 18:82 and placing it in a sealed alumina crucible and then placing it into a bigger quartz tube. After evacuating and sealing, the contents of the tube were heated to a temperature of around 1223 K for a period of 10 h, then increased again to 1433 K. The next step was to cool to 1173 K at a rate of between 1 and 2 K per hour. The final step was to quench the quartz tube in ice. At a temperature of around 250 K, $IrTe_2$ undergoes a transformation to a low temperature phase. The orbital degree of freedom is attributed to this transition since the Ir atoms' d-orbitals are partially filled. Limited replacement of Platinum for Iridium in $IrTe_2$ overwhelms the creation of the low-temperature phase, ensuing the superconductivity incidence [136,137]. Its superconductivity appears for approximately $0.04 < x < 0.14$ in $Ir_{1-x}Pt_xTe_2$. The highest $T_c$ of approximately 3.2 K is obtained at the trigonal and triclinic phase boundary when the x value is 0.04. When platinum is substituted, the Fermi level is shifted upwards. This affects the density of state near the Fermi level. The density of state is increased in the triclinic phase and decreased in the trigonal phase. The triclinic phase is also suppressed through the breakdown of the Ir-Ir dimers. Figure 16 shows the crystal structure of $IrTe_2$ at different temperatures.

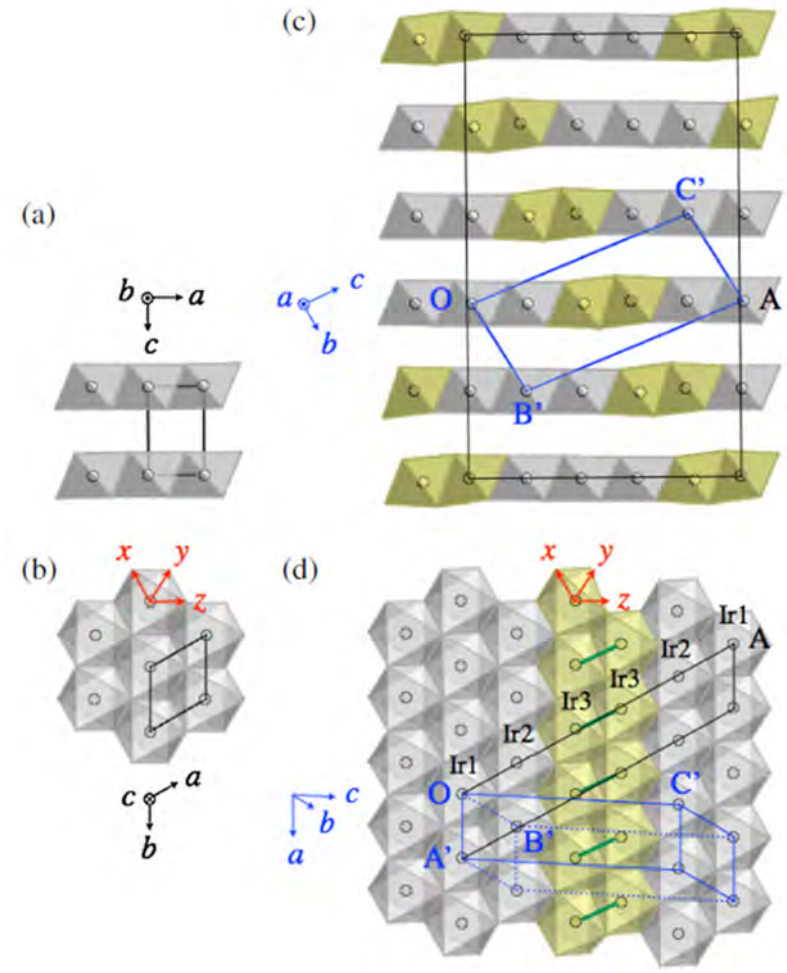


**Figure 16.** (**a**,**b**) The different views of the $IrTe_2$ crystal structure at 300 K. The trigonal lattice unit cell is shown by the black lines. (**c**,**d**) The $IrTe_2$ crystal structure at a temperature of 20 K. The blue and black lines show the triclinic lattice unit cell and the $5a \times b \times 5c$ supercell, respectively [135], where *a*, *b*, and *c* are the high-temperature trigonal-cell parameters.

Figure 17 shows the computed orbital-decomposed partial density of state for the high-temperature trigonal phase and the low-temperature triclinic phase of $IrTe_2$. Ir2 dimers formation in the low-temperature phase yields strong bonding-antibonding splitting in the $d_{yz}$ bands of the two Ir3 atoms. This makes the energy of the antibonding bands to increase above the Fermi level and reduces the energy of the bonding bands by 1 eV [135].

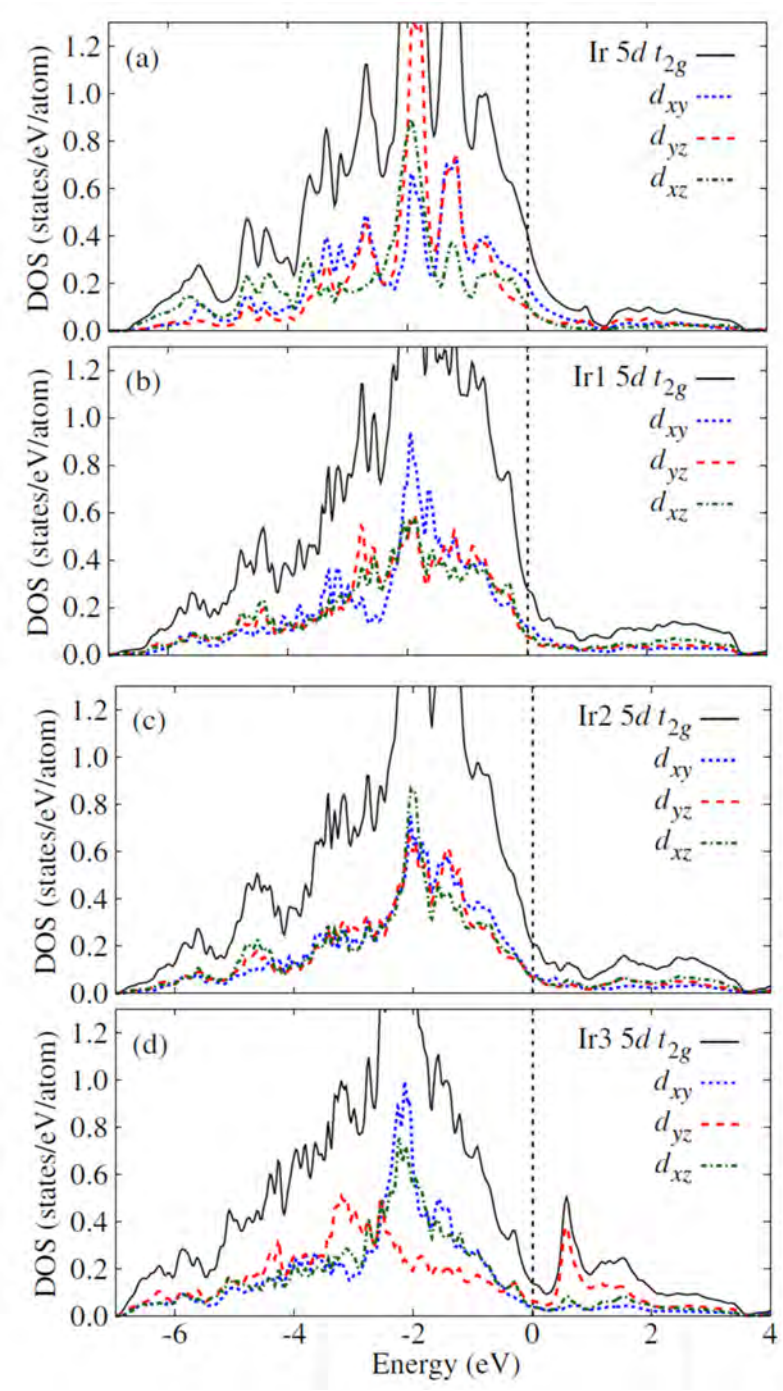


**Figure 17.** The computed orbital-decomposed partial density of state for (**a**) the high-temperature trigonal phase and the (**b**–**d**) low-temperature triclinic phase of $IrTe_2$. The dotted line is the Fermi level [135].

An example of the chalcogenide family of pyrite-type is Ir dichalcogenides $Ir_xCh_2$ (where Ch is Se or Te). The unit cell comprises of four Ir and eight Ch sites. The Iridium sites with haphazardly distributed vacancies make a simple fcc (face-centred-cubic) lattice

structure. At times it assumes the pyrite-type structures when the Iridium site vacancies are introduced [138]. High-pressure application effectively stabilises the pyrite-type form against the $Cd_2I_2$- type one [139]. Qi et al. [140] employed high-pressure synthesis technique to synthesise pyrite-type $Ir_xCh_2$ where the x value was near 1 and had transition temperature values of 6.4K and 4.7K for the two compounds $Ir_{0,91}Se_2$ and $Ir_{0,93}Te_2$, respectively. The density functional theory Qi et al. performed revealed that the compound consists of antibonding σ orbitals of the Se-Se dimer and $dz^2$ orbitals of the Ir. This meant that the transition from nonmetal to metal and the transition from metal to superconductor are driven by relaxation due to bond lengths which are alternating in the Se dimers array. Figure 18 shows the pyrite structure of $Ir_xSe_2$.

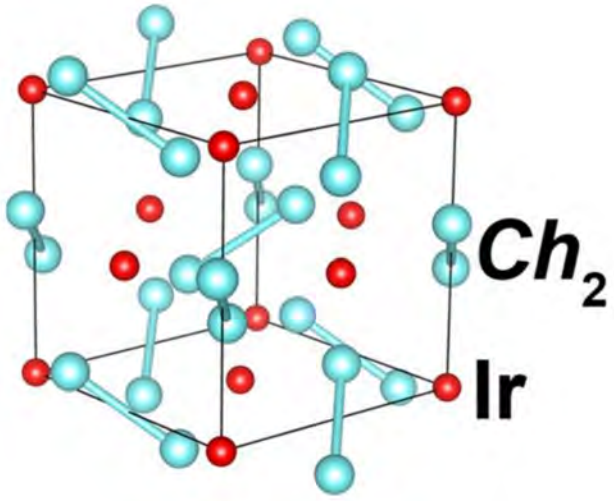


**Figure 18.** Crystal structure of pyrite $Ir_xSe_2$. The reddish-brown atoms are Ir, while the cyan colour represents Se atoms.

A noncentrosymmetric superconducting system [141–143] contains a mixture of singlet and triplet states, called a mixed parity state. $CePt_3Si$ [144], $CeCoGe_3$ [145], $CeIrSi_3$, and $CeRhSi_3$ [146] are examples of this superconductor class. The last three superconductors have a $BaNiSn_3$-type structure.

Many silicide superconductors are noncentrosymmetric, and most of them crystallise and show conventional s-wave superconductivity. The exclusions are the Cerium containing heavy-fermion compounds. Hosono et al. [54] reported on two noncentrosymmetric silicide superconductors: $SrAuSi_3$ [147] and $Li_2IrSi_3$ [148]. $SrAuSi_3$ was the first noncentrosymmetric superconductor containing gold. Gold is a heavy element that causes strong spin-orbit coupling. The stability of the $SrAuSi_3$ superconductor was found only under high pressure [147]. Figure 19 shows the crystal structure of $SrAuSi_3$. The green atoms are Sr, blue are Si atoms, and gold atoms represent Au. $SrAuSi_3$ is a relatively powerful coupling superconductor. Its $T_c$ was approximated by the McMillan formula [149–151], using the standard value of 0.13 for the Coulomb repulsion parameter μ*, resulting in a value of ∼19 K. $SrAuSi_3$ samples were synthesised using a high-pressure synthesis method at 6 GPa. The reactant powders of $SrSi_2$, Au, and Si were mixed in equal ratios in an agate mortar and then pressed into a disc which measured 6.9 mm in diameter, 3 mm in thickness, and weighed around 500 mg. The pellet was then placed in cell of high pressure (6 GPa), heated, and the temperature was kept at 1500 °C (1773 K) for an hour. Quenching to room temperature within a few seconds then followed.

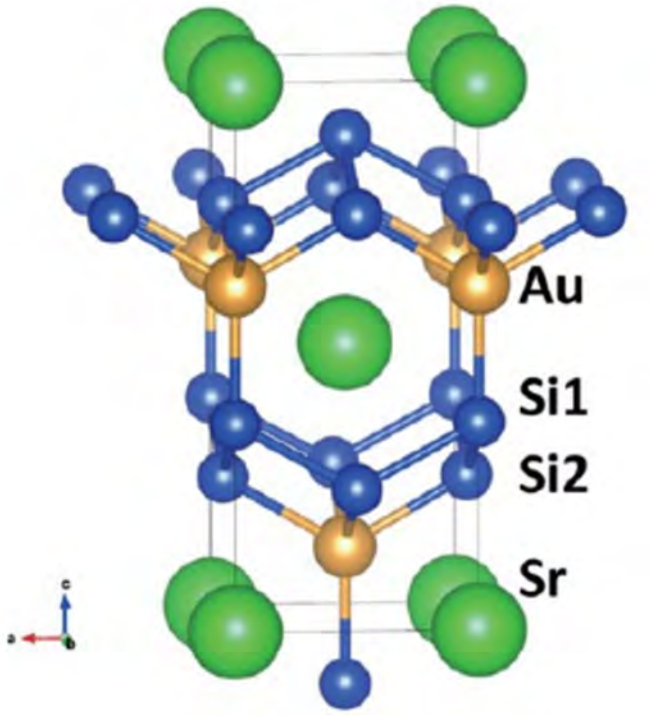


**Figure 19.** Crystal structure of $SrAuSi_3$ [147]. The structure is closely related to the $ThCr_2Si_2$ type and $CaBe_2Ge_2$ type structures.

Figure 20 illustrates the temperature reliance of resistivity quantified by fluctuating the magnetic field. The $T_c$ of $SrAuSi_3$ at zero magnetic field is 1.6 K. As the magnetic field increases, $T_c$ decreases. It gives $H_{c2}(0)$, which is approximately 2.2 kOe. This value is way lower than the Pauli limit ($H_p(0)$ of 30 kOe). Hosono et al. [54] explain that the orbital pair breaking mechanism governs $H_{c2}$. There are several other non-Fe superconductors that have been reported, such as NbSiAs ($T_c$ = 8.2 K) [152], $CeNi_{0.8}Bi_2$ ($T_c$ = 4 K) [153], LaNiBN ($T_c$ = 4.1 K), LaPtBN ($T_c$ = 6.7 K), $La_3Ni_2B_2N_3$ ($T_c$ = 15 K), $La_2Sb$ ($T_c$ = 5.3 K) [153], $Ba_{n+2}Ir_{4n}Ge_{12n+4}$ ($T_c$ = 6.1 K for n = 1; $T_c$ = 3.2 K for n = 2) [154], $Nb_4NiSi$ ($T_c$ = 7.7 K) [155], $Ti_2O_3$ [156], and $Ca_2InN$ ($T_c$ = 0.6 K) [157].

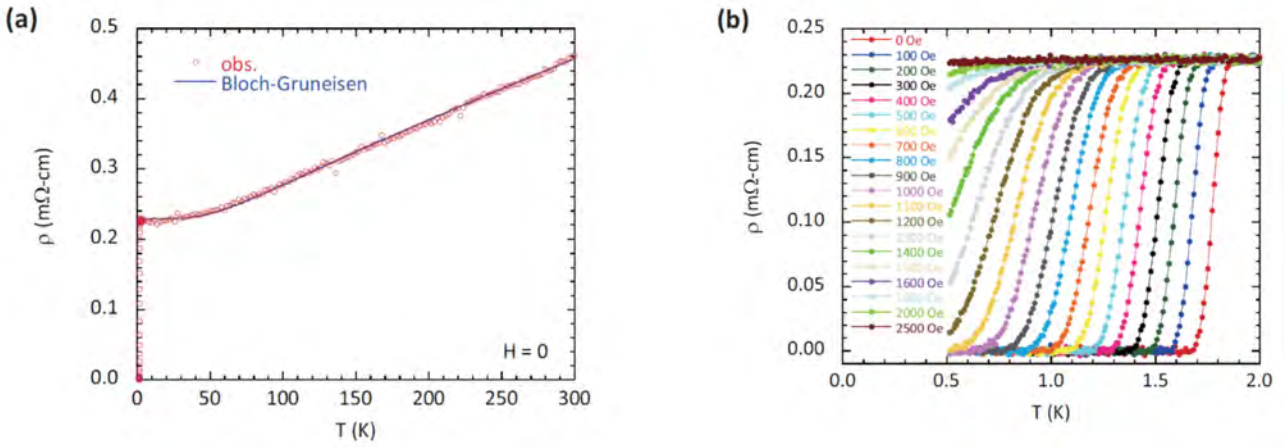


**Figure 20.** Illustration of the temperature reliance of resistivity quantified by fluctuating the magnetic field. (**a**) The $T_c$ of $SrAuSi_3$ at zero magnetic field is 1.6 K. (**b**) As the magnetic field increases, $T_c$ decreases. (**a**) is taken over a wide temperature range while (**b**) is on a narrow temperature range [54].

Cuprates are another group of other thin film superconductors that we will discuss in this review. The cuprate superconductors can be fabricated by pulsed laser deposition (PLD), laser ablation and dc magnetron sputtering.

In 2017, Arpaia et al. [158] reported on the fabrication of ultrathin$YBa_2Cu_3O_{7-\delta}$ (YBCO) films on a magnesium oxide substrate using the PLD technique from thicknesses ranging between 50 and 3 nm. Their deposition conditions were a temperature of 760 °C and an oxygen pressure of 0.7 mbar. After the deposition process, the deposited material was cooled at a rate of 5 °C/min. The group used atomic force microscopy (AFM) to perform morphological and structural characterisation. Scanning electron microscopy (SEM) and x-ray diffraction (XRD) were utilised to determine the film quality and structural properties, respectively. The team reported that the onset temperature of the superconducting transition slightly changes with the thickness of the film, while the zero-resistance temperature significantly decreases when reducing the film thickness. The lower onset transition temperature was attributed to both an increase and a decrease in oxygen doping in the film. Figure 21 shows the temperature versus resistance curve of YBCO thin films where the thickness values are 10, 20, and 50 nm.

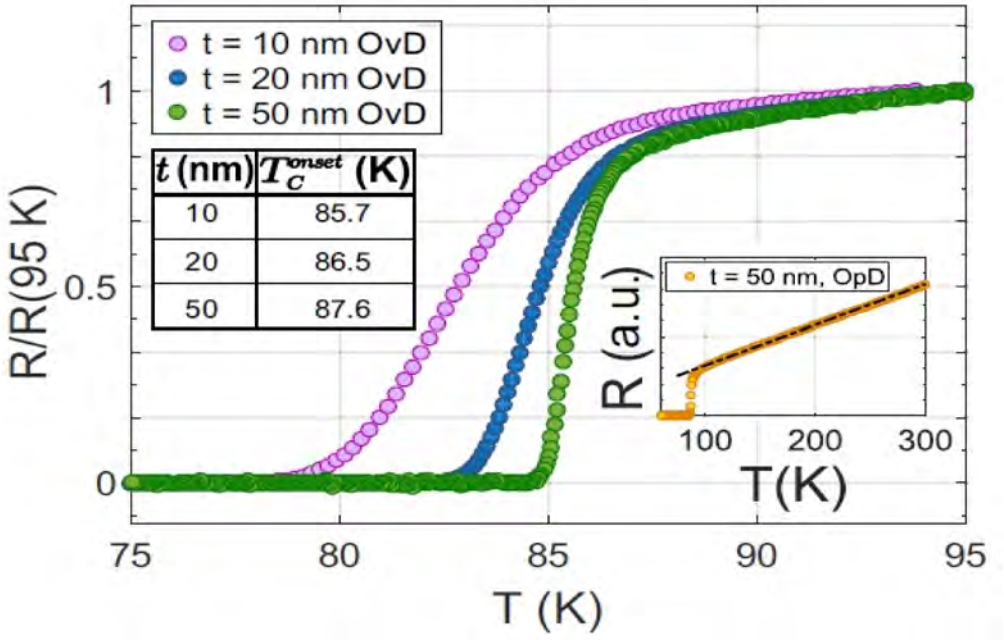


**Figure 21.** Resistance vs. temperature curve of YBCO thin films where the thickness values are 10, 20, and 50 nm. The insert table shows the values of the calculated onset transition temperature for the three thicknesses. The insert on the right shows the temperature versus resistance measurement of an optically doped 50 nm bare thin film whose onset transition temperature was 89.1 K [158].

Stepantsov et al. [159] reported on the growth of superconductive $YBa_2Cu_3O_{7-x}$ thin films of b orientation on the surface of a $SrLaGaO_4$ crystal using the Czochralski technique. The team deposited a buffer layer of $PrBa_2Cu_3O_{7-x}$ of 60 nm thickness onto the substrate surface using the rf sputtering technique. The chamber was filled with oxygen and argon gas mixture in a ratio of 1 to 4 up to a pressure of 0.1 mbars. The temperature of the substrate was raised to 600–750 °C while a 50 W rf discharge was applied between the target and the substrate. The chamber was then filled with pure oxygen to a pressure of 600 mbars and the substrate with the deposited film was annealed at 550 °C for an hour, after that it was cooled to room temperature. The chamber was then evacuated and replaced with a PLD chamber where the $YBa_2Cu_3O_{7-x}$ was grown. The team reported that the film is free of any other domains of crystallographic orientations of the intrinsic material, which includes the a-oriented component. Figure 22 shows the resistance vs. temperature curve for $YBa_2Cu_3O_{7-x}$.

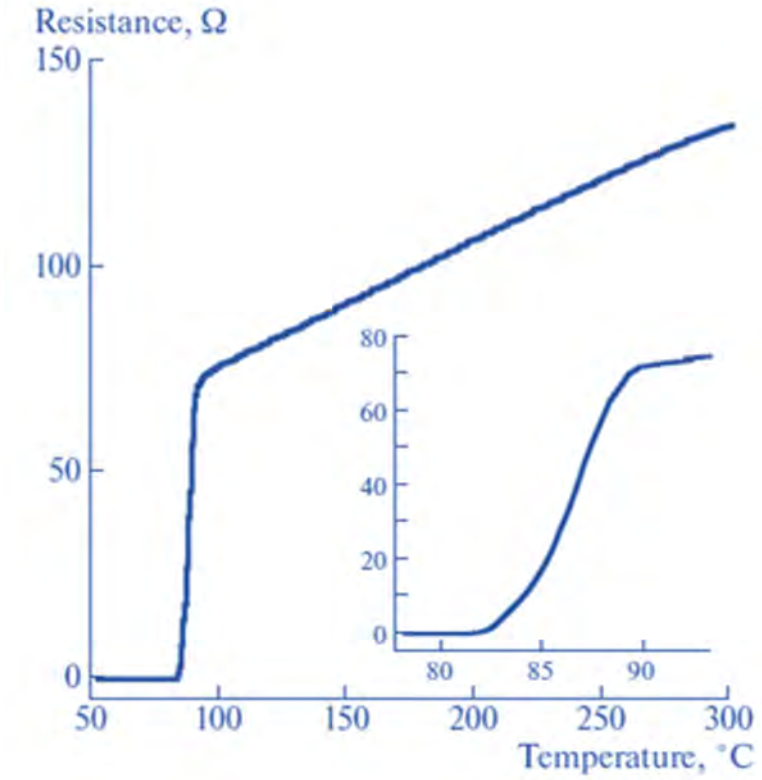


**Figure 22.** Resistance vs. temperature curve of a b-oriented $YBa_2Cu_3O_{7-x}$ film grown on a substrate of $SrLaGaO_4$.

Stepantsov et al. [160] reported on the fabrication of superconductive $YBa_2Cu_3O_7$ thin-films with tilt CuO [100] planes to the surface on $SrTiO_3$ substrate, using the pulsed laser deposition technique. The $SrTiO_3$ single crystals, which were prepared by the Verneuil technique, were x-ray oriented, cut, and polished by a chemical-mechanical method to obtain substrates with one of the [100]—type planes tilted to the surface by 0 to 70° in 5° increments. $YBa_2Cu_3O_7$ was then grown on these substrates by PLD. The team used the four circle Philips X'Pert Xray diffractometer to study the structure of the films. They found that $YBa_2Cu_3O_7$ (YBCO) grown on the $SrTiO_3$ was a single crystal with the (014) face oriented parallel to the surface. They also reported that $YBa_2Cu_3O_7$ thin-films with CuO planes tilted to the surface by up to 41° can be deposited on the $SrTiO_3$ crystal surface [160].

Kislinskii et al. [161] reported on the production of direct current superconducting quantum interference devices (dc SQUIDS) and Josephson junctions using $YBa_2Cu_3O_7$ thin-films, which were deposited on $ZrO_2$ bi-crystal substrates stabilised by yttrium, using laser ablation and dc magnetron sputtering. The team used a strip with a width of 30 μm to measure critical transition temperature and critical density of the films. The strip had been patterned by chemical etching. The deposited thin films had a $T_c$ of 90 K and critical current density of approximately $2 \times 10^6$ A/cm$^2$. The voltage modulation depth of this SQUID was 6 μV. Figure 23 shows the voltage–current characteristic curves for the yttrium stabilised $ZrO_2$ and YBCO.

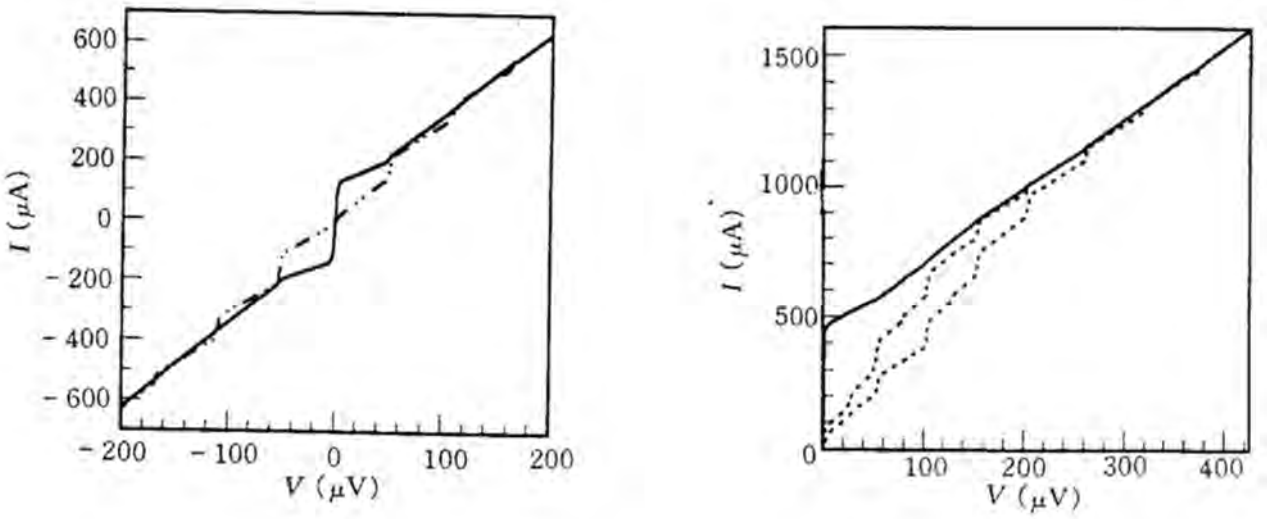


**Figure 23.** (**Left**) I–V characteristics of the Josephson junction on the 28° misoriented yttrium stabilised $ZrO_2$ bi-crystal without (represented by solid line) and with microwave radiation of 23.4 GHz (represented by broken line) at a temperature of 77 K. (**Right**) I–V curves for the 28° misoriented weak link of YBCO at different levels of 23.4 GHz microwave power (dotted lines) and without radiation (solid line) at 62 K.

Carillo et al. [162] reported on the resistance magneto-fluctuation measurements and proximity-effect in $Nd_{1.2}Ba_{1.8}Cu_3O_z$ (NBCO) to analyse the coherent charge transport in the non-superconducting state. The team discovered an unanticipated inhibition of Cooper pair transport, and the disappearance of superconductivity when the temperature was lowered from 6 K to 250 mK. Their magnetoconductance and conductance measurements pointed to the mechanism of pair breaking at temperatures lower than 2 K. In their investigation, the team showed a transition of an underdoped NBCO nanostructure from a temperature above 2–3 K where Cooper pair transport is permitted, to a lower temperature where the Cooper pairs are not permitted to flow.

Chaix et al. [163] reported on dispersive charge density wave excitations in $Bi_2Sr_2CaCu_2O_{8+\delta}$. The team A new charge density wave (CDW) modulation was unearthed in underdoped $Bi_{2.2}Sr_{1.8}Ca_{0.8}Dy_{0.2}Cu_2O_{8+\delta}$ using ultrahigh resolution resonant inelastic X-ray scattering. Dispersive excitations were observed from an incommensurate charge density wave at low temperatures, which the enhanced phonon intensity. The CDW persisted near the pseudogap temperature, but other excitations drastically weakened, signalling a charge density wavevector shift. The phonon anomaly, dispersive CDW excitations and CDW wavevector analysis provided a momentum-space understanding of complex CDW behaviour. Figure 24 shows the temperature dependence of the charge density wave and the phonon anomaly.

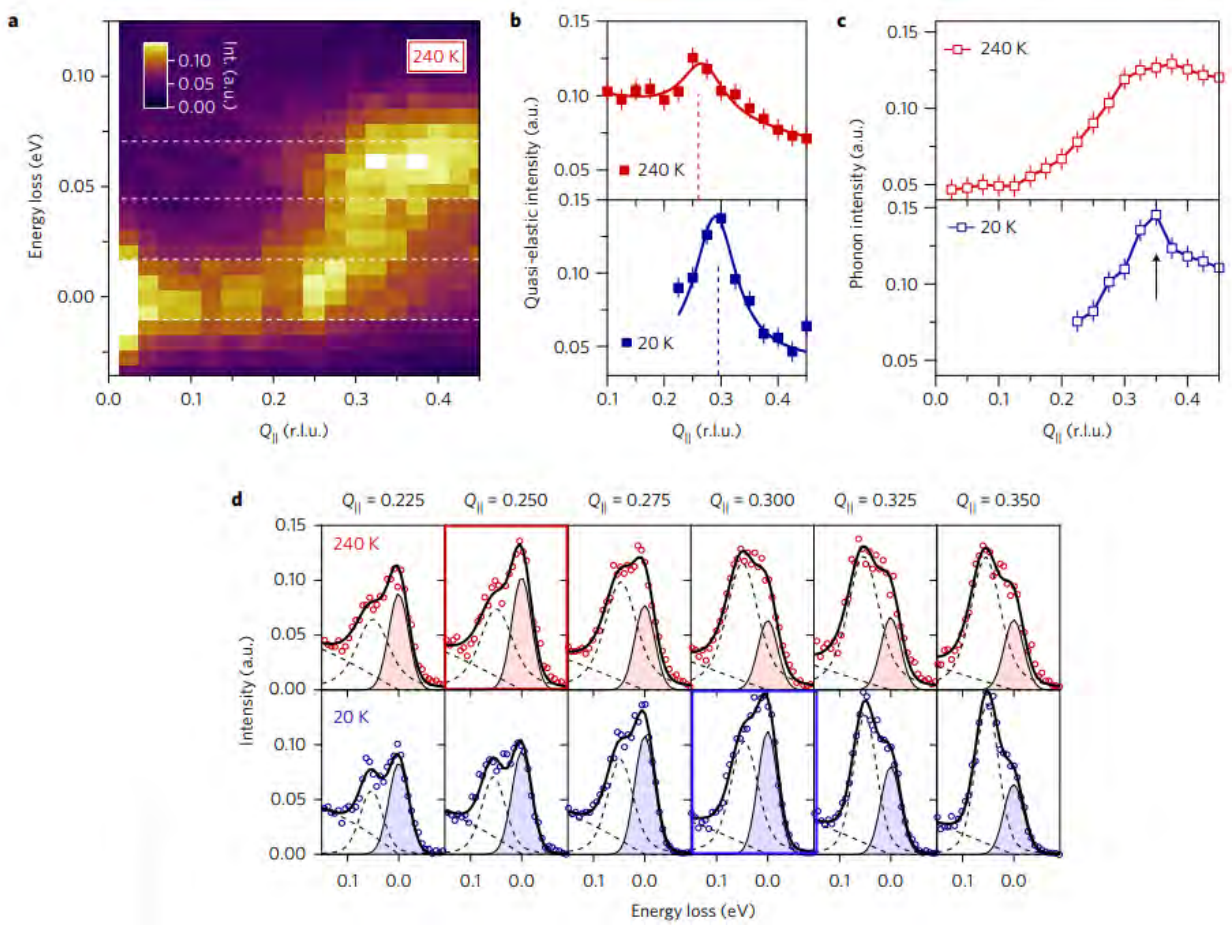


**Figure 24.** Temperature dependence of the charge density wave and the phonon anomaly. (**a**) RIXS intensity map taken at a temperature of 240 K. The quasi-elastic region (centred at zero energy loss) and the phonon energy region (centred at 60 meV) used for computing the mean intensity profile shown in (**b**,**c**) are defined by the white dashed line. (**b**) Averaged intensity of the quasi-elastic region (indicated in (**a**)) at 240 K (red) and 20 K (blue). The dashed lines indicate the position of the charge density wave. (**c**) Mean phonon energy regions intensity as defined in (**a**), at 240 K and 20 K. The black arrow highlights the intensity anomaly at 20 K. Error bars in (**b**,**c**) are estimated by the noise level of the spectra. (**d**) Raw energy-loss spectra (markers) and the corresponding fits (solid lines) of RIXS data taken at T = 240 K (at the top) and T = 20 K (at the bottom). Filled areas highlight elastic peak fits. Red and blue boxes for T = 240 K and T = 20 K, respectively, represent the RIXS spectra where the elastic peak intensity is maximal (that is, the CDW position).

## 3. Atomic Layer Deposition in the Synthesis of Thin Film Superconductors

Atomic layer deposition [164–173] is a growing deposition technique used to synthesise thin-film superconductors due to its precise and uniform atomic thickness control [174]. The process is mainly applied to grow thin film oxides. Amongst the different thin film fabrication processes, atomic layer deposition [164,165,175–180] has steadily grown in the past decade to be the preferred thin-film manufacturing process. Atomic layer deposition has several advantages over the other fabrication techniques, like precise deposited material atomic thickness control, homogeneousness of thicknesses deposited even on complex three-dimensional surfaces, relatively lower system temperatures, and improved electronic properties of devices [174].

In the following few paragraphs, we look at selected publications where ALD has been used to synthesise thin-film superconductors.

Sowa et al. [181,182] used plasma-enhanced atomic layer deposition to synthesise superconducting niobium nitride. The niobium precursor the team used was (t-butylimido)

tris(diethylamido) niobium(V), abbreviated as TBTDEN. This precursor was kept at a temperature of 373 K and introduced into the reactor with a precursor Boost system. In this system, a charge of argon gas is introduced into the cylinder of the precursor before the precursor is pulsed into the atomic layer deposition reactor. This enhances low vapour material transfer to the surface of the substrate. The nitrogen precursor was the $H_2/N_2$ plasma. The substrate used was prime silicon and silicon, which had a layer of 1 μm of silicon dioxide that was thermally grown. The substrate temperature was kept between 373 K and 573 K. NbN thin films have several applications, which include hard surface coatings, [183–185] gate electrode metal, [32,186–190] copper interconnect diffusion barrier, [188–190], and other applications that exploit the material's superconducting properties [30,191–200]. Superconductivity measurements were carried out using the standard AC lock-in method. Room temperature resistivities as low as 173 μΩcm and $T_c$ value of 13.7 K were observed. Figure 25 shows the resistance (R) and magnetisation moment plots of NbN thin films. X-ray reflectivity (XRR) measurements showed that thin film NbN thin films have a lower density of between 6.4 and 7.8 g/cm$^3$ compared with the bulk density of NbN whose value is 8.47 g/cm$^3$. Figure 26 shows the various density measurements under different conditions.

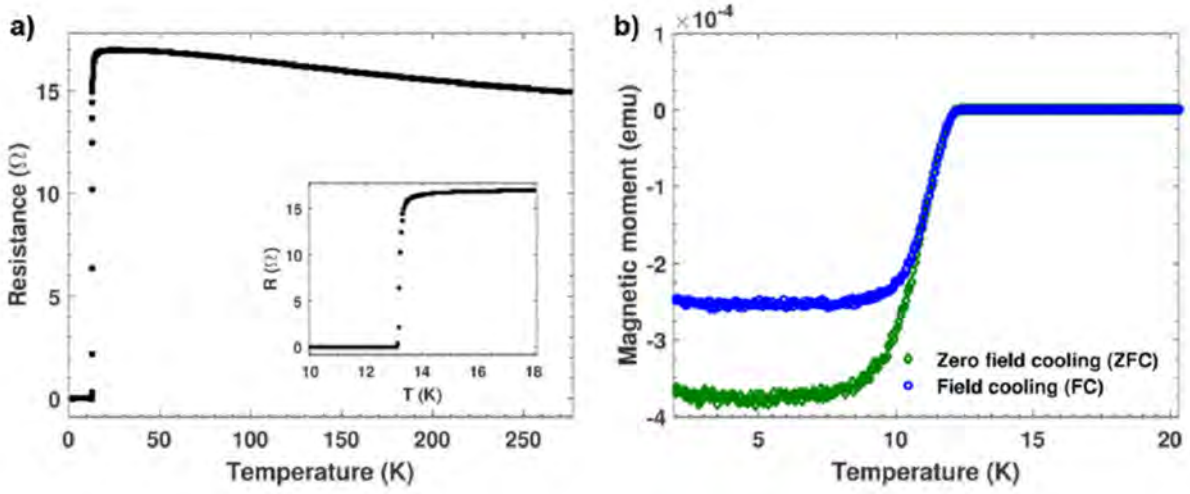


**Figure 25.** Resistance and magnetisation moment plots for NbN films. (**a**) R vs. T for the measurement $T_c$ and (**b**) magnetisation plot of Niobium Nitride film deposited at 573 K, 40 sccm $H_2$, and 300 W of power [181].

Tamm et al. [201] used ALD to deposit superconducting CuO thin films. They used copper (II)-bis-(-dimethylamino-2-propoxide), a metal-organic precursor, and ozone as an oxidiser. The pressure conditions employed were between 200 and 260 Pa. The copper precursor vapourisation temperatures ranged between 81 and 87 °C (354 and 360 K). The BMT Messtechnik 802 N generator was used to produce ozone from oxygen. The substrate, Si (100) temperature was kept between 112 and 160 °C (385 and 433 K). CuO was the resulting copper oxide phase in this temperature range. They employed two-probe electrical resistivity measurements, which discovered a drop of resistivity below $T_c$ of 4 K. This indicated low-temperature Takeshi in the thin films of copper oxide. Nb/Cu thin film cavities are still used in several superconducting radio frequency (SRF) accelerators. Figure 27 shows the resistivity plots at various temperatures.

Klug et al. [194] employed ALD to deposit amorphous Niobium Carbide-based thin-film superconductors. They used trimethylaluminum (TMA) [$Al(CH_3)_3$], Niobium pentafluoride and Niobium pentachloride precursors. Klug et al. characterised the film thickness, composition, structure, and morphology by scanning electron microscopy (SEM), X-ray photoemission spectroscopy (XPS), Rutherford backscattering spectroscopy (RBS), X-ray reflectivity (XRR), atomic force microscopy (AFM), X-ray diffraction (XRD), and transmis-

sion electron microscopy (TEM). Superconducting quantum interference device (SQUID) magnetometry measurements showed a transition into superconductivity at $T_c$ = 1.8 K in a 75-nanometre thick film synthesised at a temperature of 350 °C. The team also noted that superconducting $T_c$ might be improved to 3.8 K when $NH_3$ is used during atomic layer deposition film growth. Figure 28 shows the X-ray photoemission spectroscopy analysis of the Al 2p, C 1s, F 1s, and Nb 3d peaks at different temperatures.

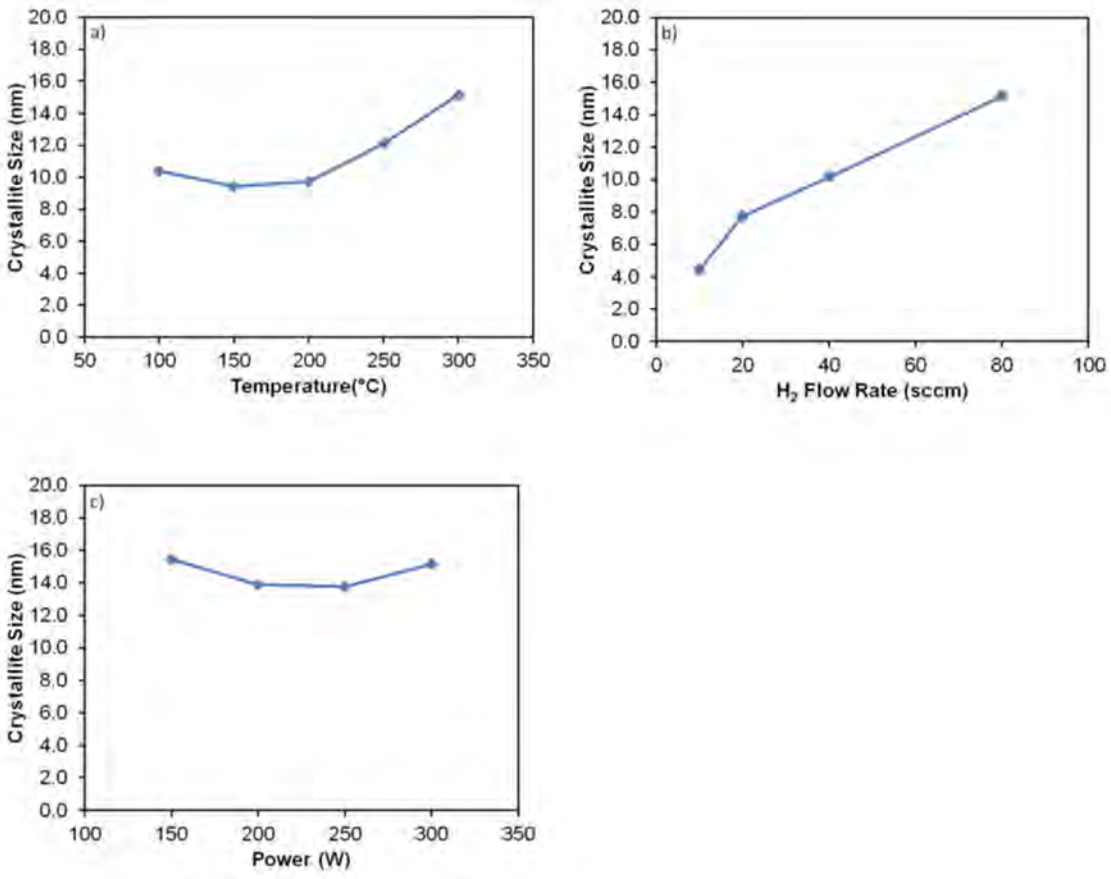


**Figure 26.** Effects of (**a**) temperature, (**b**) $H_2$ flow rate, and (**c**) power variations on the NbN thin film density [181].

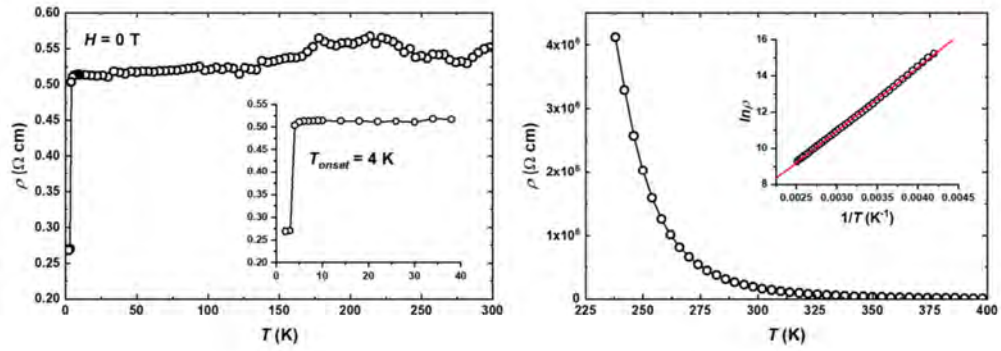


**Figure 27.** Resistivity against temperature plots from two-probe electrical resistivity measurements for various temperatures. The onset of superconductivity started just before 4 K [201].

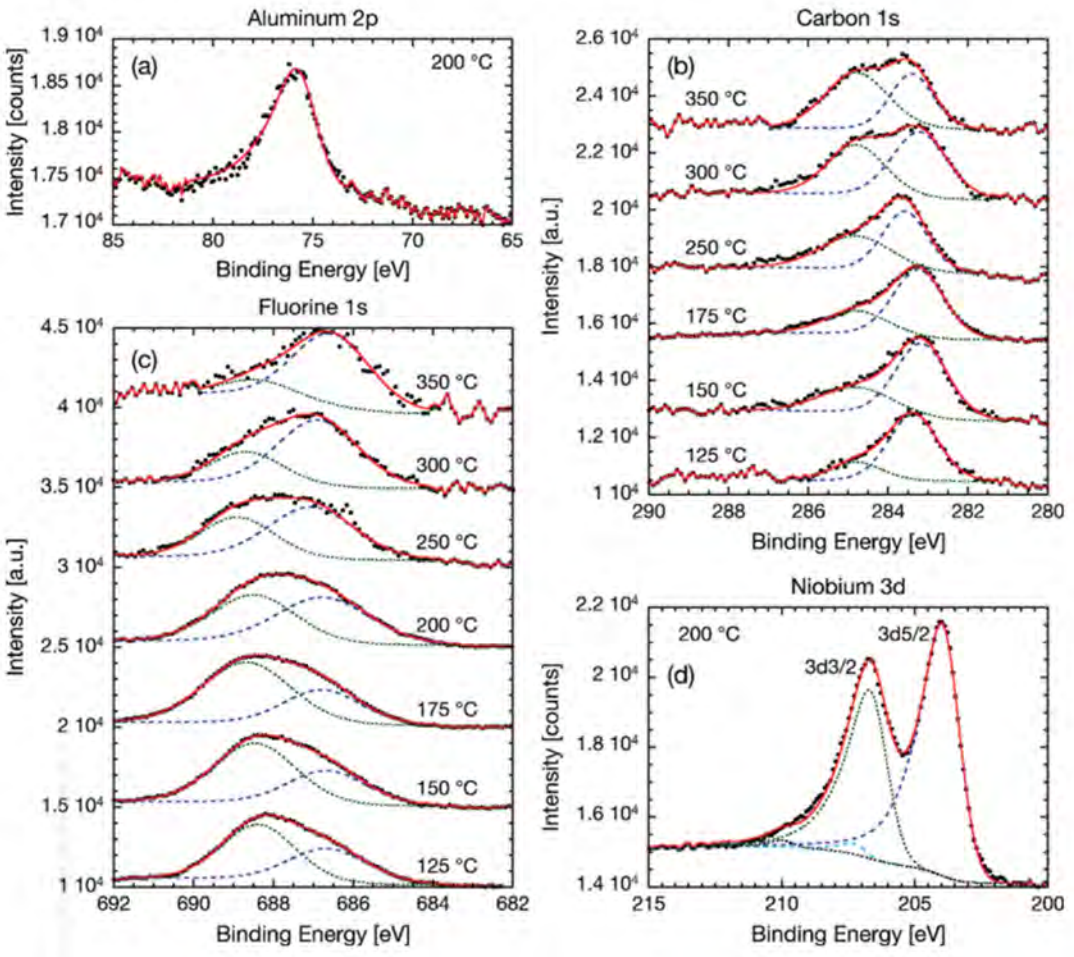


**Figure 28.** Detailed X-ray photoemission spectroscopy analysis of the (**a**) aluminum 2p, (**b**) carbon 1s, (**c**) fluorine 1s, and (**d**) niobium 3d peaks at different temperatures with TMA and $NbF_5$ [194].

Shibalov et al. [170] reported on a multistep ALD technique for superconducting Niobium Nitride ultrathin films [202] with high critical current density on the amorphous substrate. They synthesised superconducting ultrathin NbN films using tris(diethylamido)(tert-butylimido) niobium (V), $NH_3$/Ar, and $H_2$/Ar gas mixtures as reactants and amorphous $SiO_2$ as their substrate. The team conducted a broad analysis relating to the effect of operating parameters, like the extent of plasma exposure to the $H_2$/Ar reactant, duration of plasma exposure, gas-flow proportion, and inductively coupled plasma source power for the $NH_3$/Ar reactant, on the obtained films' parameters, which include $T_c$, critical current density, and resistivity. They achieved a resistivity of 147 μΩ·cm for 8 nanometres thick films. Cooling in the Gifford McMahon closed-cycle cryostat yielded a $T_c$ value of 12.3 K and $J_c$ (critical current density) of 9 MA/cm$^2$ at a liquid He temperature [170]. NbN thin film are used in superconducting radio frequency (SRF) accelerators.

Yemane et al. [182] reported on superconducting NbTiN thin films synthesised by plasma-enhanced ALD. NbTiN has several superconducting applications, such as RF cavities, single-photon detectors, superconductor–insulator–superconductor (SIS) mixers, and hot-electron bolometers. Compared to NbN, NbTiN has a lower secondary emission coefficient and sensitivity to radiation, which makes it preferable for generating higher accelerating fields in superconducting radio frequency (SRF) applications. Yemane and colleagues explored the PEALD of $Nb_xTi_{1-x}N$ using organometallic precursors (t-butylimido) tris(diethyamido) niobium (V) and tetrakis (dimethylamido) titanium together with a remote $H_2/N_2$ plasma. The control of film composition permitted them to tune the electrical and superconducting characteristics, like fluctuating $T_c$ between the values of 6.9 K

and 13.2 K. Thin films produced through the sputtering process were produced at 600 °C and showed higher $T_c$ values. Although this was the case, the much lower temperatures (300 °C for the reactor and between 75 and 100 °C for the substrate) used in PEALD makes it more preferable.

## 4. Current and Future Applications of Superconductors

Some applications of individual superconductors were mentioned in this review when such superconductors were discussed. The following is a brief description of the uses and applications of superconductors.

Large Hadron Collider particles are accelerated using superconducting magnets [203]. The Large Hadron Collider is the biggest particle accelerator located at the CERN laboratory near Geneva in Switzerland. There are two particle beams of very high energy inside the accelerator that travel at a speed close to that of light. Superconducting magnets (made from NbTi superconductors) are used to keep the beams apart in separate beam pipes before they are made to collide. The cooling medium for the large hadron collider is liquid Helium. The operating temperature of the magnets is around 1.9 K. The Large Hadron Collider was designed to help scientists and engineers understand the structure of matter in the first few moments of the universe before the big bang. It re-models those extreme conditions according to the big bang theory [204]. The Large Hadron Collider is credited for the discovery of the Higgs boson, which gives mass to all other fundamental particles.

SQUIDs (superconducting quantum interference devices) are utilised in the synthesis of extremely sensitive magnetometers, which are used to detect land mines [18,53,194,205,206]. They have also found applications in engineering, geological equipment, and medical instruments where extreme sensitivity is required. SQUIDs are used to measure low and weak magnetic fields, as low as $5\times10^{-14}$ T. It comprises two superconductors that are kept apart by very thin insulating layers, forming two parallel Josephson junctions. The main superconductors used in SQUIDs are either a lead alloy, which contains about 10% indium or gold, or niobium superconductors. Yttrium barium copper oxide superconductors (YBCO) ($YBa_2Cu_3O_7$) can also be used [207].

Magnetic Resonance Imaging (MRI) machines use superconducting magnets [206]. This is a method to scan the whole body, as the solenoids can create large uniform magnetic fields [208]. The strong magnetic field from the superconducting magnets force the photons in the body to align to their magnetic field. Pulsing a radiofrequency current stimulates the photons and causes them to spin out of equilibrium. Turning off this current causes the photons to release energy as they realign with the magnetic field. The amount of energy released by the photons is detected by the MRI sensors. This enables the physicists to identify the type of tissue based on the magnetic properties. MRI scans are used to create detailed images of tissues and body organs. Just like in the Large Hadron Collider, the MRI uses niobium titanium superconductors [209].

Superconducting cables are yet to be commercially applied extensively to replace ordinary cable lines to transport power over long distances without any power loss [210]. Superconductive cables would prevent much energy losses and carry large quantities of currents compared with the same volumes of copper and aluminium cables [211].

Superconductors are also being utilised in advance of high-intensity Electro-Magnetic Pulse (EMP) [212], which is employed for paralysing all the electronic equipment within its range.

Maglev (magnetic levitation) trains [206] in Japan work on the superconducting magnetic levitation phenomenon. Niobium Titanium superconductors are used as the superconducting magnets. Magnetic levitation is the phenomenon whereby two magnetic materials are repelled from each other in a vertical direction, enabling one to be suspended over another by powerful electromagnetic forces only. Maglev trains use superconducting magnets onboard the train and levitation coils on the railway track and sidewalls of the guide way. Magnetic levitation and propulsion are used to lift, propel, and guide the train over its track.

## 5. Superconductor Technology Challenges

Superconductivity becomes a qualifying technology when magnetic fields above 3T need to cover huge apertures (for example, 10 cm in the final bend of the upstream scanning gantry) [203]. In the following few paragraphs, we discuss the challenges faced by the thin film superconductor technology.

Superconductors produce strong electromagnetic fields in the magnets; hence, very heavy mechanical structures are needed to counter the impact of Lorentz forces in order to bring about mechanical stability. The strong Lorentz forces have the potential to rapture some machine components. The large mechanical structures required add to the total weight of the machine [203].

The strong fields of the gantry magnets positioned close to the patient can result in more prolonged and powerful stray fields; this inhibits the proper functioning of other health equipment that can be affected by magnetic fields. The health safety guidelines for magnetic resonance imaging equipment in clinical use states that at the patient location, the field must be less than 0.5 mT. Shielding of the magnetic fields in the instruments is required.

The superconducting state [28,115,144,213,214] is governed by a blend of three constraints: magnetic field ($H_c$), current density ($J_c$), and temperature ($T_c$). Temperature is the most difficult parameter to regulate because of the nearly 100% efficiency of the ultimate change of the magnetic and mechanical energy stored in the magnet to heat energy. When one of these three critical parameters ($J_c$, $H_{c2}$, $T_c$) is exceeded, a quench in the magnet may be produced. The outcome of this quench is reduced reliability.

The servicing of superconductive magnets might be difficult and require devoted highly skilled technical team responsible for the maintenance of the equipment [203]. The maintenance of helium tanks for cooling the magnets and their subsequent refilling also come at a cost.

Power applications of superconductivity lack a "compelling need" associated with either current or forthcoming energy societies, since the present technologies perform acceptably. High-temperature superconductor (HTSC) technology now "sit on the shelf", anticipating use in case it proves economically viable to use it [215].

Room temperature superconductors that have been synthesised require very high pressures for them to attain superconductivity at room temperature. This is a significant cost that makes them economically unviable. A room-temperature superconductor at atmospheric pressure is yet to be synthesised.

## 6. Conclusions

The discovery of superconductivity in 1911 drew wide interest and excitement from engineering and materials science fields. Various superconductors have been manufactured ever since. Superconductors are basically either of two types: Type I and Type II. Type II superconductors can be further classified into high temperature and low temperature superconductors, and conventional BCS superconductors and non-conventional BCS superconductors. Methods of fabricating thin-film superconductors include molecular beam epitaxy, pulsed layer deposition, and atomic layer deposition. Some bulk superconductor manufacturing technologies include conventional solid-state reaction method, self-flux technique, high pressure high temperature synthesis technique, and arc melting technique. The superconducting transition temperature of thin films changes with the film thickness; hence it can affect the overall superconducting behaviour of the deposited material. The growth of thin films is an extremely active process where the kinetics that take place during nucleation and the microscopic level growth are the crucial defining aspects for the resultant structure, morphology, and characteristics of the thin film. Because of the need for precise thickness control of thin films of superconductors, atomic layer deposition is one of the widely used techniques in the manufacture of superconductors. This review has deliberately put more emphasis on atomic layer deposition as a thin film fabrication technique because of the recent interest it has gained amongst researchers in the past

decade. There are various applications of thin film superconductors which include gate electrode metal, copper interconnect diffusion barrier, MRI machines, SQUIDs, Maglev trains, Electro-Magnetic Pulse, among others. The thin-film technology offers a lucrative scheme of creating engineered surfaces and opens a wide exploration of prospects to modify material properties for specific applications, such as those which depend on surfaces. Although superconductors are applied practically in various fields, their application is hindered by the need to cool the material to very low temperatures; hence their applications are growing slower than expected.

**Author Contributions:** D.S.: Conceptualization, Methodology, Investigation, Visualization, Writing—original draft; S.T.O.: Formal analysis, review and editing, visualization, supervision; A.I.I.: Visualization, Writing—original draft; T.-C.J.: Resources, Supervision, Formal analysis, Validation, Project administration. All authors have read and agreed to the published version of the manuscript.

**Funding:** This research received no external funding.

**Acknowledgments:** The authors would like to thank the financial support from University Research Committee of the University of Johannesburg, and Jen would like to acknowledge the financial support from National Research Foundation of South Africa.

**Conflicts of Interest:** The authors declare no conflict of interest.

## References

1. Hott, R.; Kleiner, R.; Wolf, T.; Zwicknagl, G. Review on Superconducting Materials. *Arxiv Prepr.* **2013**, arXiv:1306.0429. [CrossRef]
2. Cuo, L.A.; Green, B. Superconducting Phases in Bulk and Thin Film $LA_2$ $CuO_4$. *Undergrad. Rev.* **2008**, *4*, 85–92.
3. Ruan, B.-B.; Zhao, K.; Mu, Q.-G.; Pan, B.-J.; Liu, T.; Yang, H.-X.; Li, J.-Q.; Chen, G.-F.; Ren, Z.-A. Superconductivity in Bi3O2S2Cl with Bi–Cl Planar Layers. *J. Am. Chem. Soc.* **2019**, *141*, 3404–3408. [CrossRef] [PubMed]
4. Asaba, T.; Wang, Y.; Li, G.; Xiang, Z.; Tinsman, C.; Chen, L.; Zhou, S.; Zhao, S.; Laleyan, D.; Li, Y.; et al. Magnetic Field Enhanced Superconductivity in Epitaxial Thin Film $WTe_2$. *Sci. Rep.* **2018**, *8*, 6520. [CrossRef] [PubMed]
5. Bennernann, K.H.; Ketterson, J. *The Physics of Superconductors: Conventional and High-Tc Superconductors*; Springer: Berlin/Heidelberg, Germany, 2003.
6. Lundy, D.R.; Swartzendruber, L.J.; Bennett, L. A BriefReview of Recent Superconductivity Research at NIST. *J. Res. Natl. Inst. Stand Technol.* **1989**, *94*, 147–174. [CrossRef] [PubMed]
7. Bardeen, J.; Cooper, L.N.; Schrieffer, J. Theory of Superconductivity. *J. Phys.* **1957**, *108*, 1175–1204. [CrossRef]
8. London, F.; London, H. The electromagnetic equations of the supraconductor. *Proc. Roy. Soc.* **1934**, *85*, 71–88.
9. Kogan, V.; Nakagawa, N. Moving Pearl Vortices in Thin-Film Superconductors. *Condens. Matter* **2021**, *6*, 4. [CrossRef]
10. Gelens, L.; Matías, M.A.; Gomila, D.; Dorissen, T.; Colet, P. Formation of localized structures in bistable systems through nonlocal spatial coupling. II. the nonlocal Ginzburg-Landau equation. *Phys. Rev. E* **2014**, *89*, 012915. [CrossRef]
11. Ginzburg, V.L.; Landau, L.D. On the Theory of superconductivity. *Zh. Eksperim. Teor. Fiz.* **1950**, *20*, 1064–1082.
12. Flores-Livas, J.A.; Boeri, L.; Sanna, A.; Profeta, G.; Arita, R.; Eremets, M. A perspective on conventional high-temperature superconductors at high pressure: Methods and materials. *Phys. Rep.* **2020**, *856*, 1–78. [CrossRef]
13. Bennemann, K.H.; Ketterson, J. *The Physics of Superconductors: Superconductivity in Nanostructures, High-Tc and Novel Superconductors, Organic Superconductors*; Springer: Berlin/Heidelberg, Germany, 2004.
14. Jha, A.K.; Matsumoto, K. Superconductive REBCO Thin Films and Their Nanocomposites: The Role of Rare-Earth Oxides in Promoting Sustainable Energy. *Front. Phys.* **2019**, *7*, 1–21. [CrossRef]
15. Zhang, C.; Hao, F.; Gao, G.; Liu, X.; Ma, C.; Lin, Y.; Yin, Y.; Li, X. Enhanced superconductivity in TiO epitaxial thin films. *npj Quantum Mater.* **2017**, *2*, 2. [CrossRef]
16. Agafonov, A.I. Finding the boson-number distributions in superconducting thin-film rings. *Int. J. Mod. Phys. B* **2014**, *28*, 1–15. [CrossRef]
17. Vestgården, J.I.; Johansen, T.H.; Galperin, Y.M. Nucleation and propagation of thermomagnetic avalanches in thin-film superconductors (Review Article). *Low Temp. Phys.* **2018**, *44*, 460–476. [CrossRef]
18. Antoine, C.Z.; Berry, S.; Bouat, S.; Jacquot, J.-F.; Villégier, J.-C.; Lamura, G.; Gurevich, A. Characterization of superconducting nanometric multilayer samples for superconducting rf applications: First evidence of magnetic screening effect. *Phys. Rev. Spéc. Top. Accel. Beams* **2010**, *13*, 121001. [CrossRef]
19. Stewart, G.R. Unconventional superconductivity. *Adv. Phys.* **2017**, *66*, 75–196. [CrossRef]
20. Fernandes, R.M.; Conde-Gallardo, A.; Ayón-Beato, E.; Godina-Nava, J.J.; Hernández-Contreras, M.; Velasco-Sevilla, L. Conventional and unconventional superconductivity. *AIP Conf. Proc.* **2012**, *1420*, 135–144. [CrossRef]
21. Sakoda, M.; Iida, K.; Naito, M. Recent progress in thin-film growth of Fe-based superconductors: Superior superconductivity achieved by thin films. *Supercond. Sci. Technol.* **2018**, *31*, 093001. [CrossRef]

22. Huebener, R. *Conductors, Semiconductors and Superconductors: An Introduction to Solid State Physics*, 2nd ed.; Springer International Publishing: Cham, Switzerland, 2016.
23. Zhi-An, R.; Wei, L.; Jie, Y.; Wei, Y.; Xiao-Li, S.; Zheng, C. Superconductivity at 55 K in Iron-Based F-Doped Layered Quaternary Compound SmFeAs. *Chin. Phys. Lett.* **2008**, *25*, 2215. [CrossRef]
24. Watanabe, T.; Yanagi, H.; Kamihara, Y.; Kamiya, T.; Hirano, M.; Hosono, H. Nickel-based layered superconductor, LaNiOAs. *J. Solid State Chem.* **2008**, *181*, 2117–2120. [CrossRef]
25. Nobukane, H.; Yanagihara, K.; Kunisada, Y.; Ogasawara, Y.; Isono, K.; Nomura, K.; Tanahashi, K.; Nomura, T.; Akiyama, T.; Tanda, S. Co-appearance of superconductivity and ferromagnetism in a $Ca_2RuO_4$ nanofilm crystal. *Sci. Rep.* **2020**, *10*, 3462. [CrossRef]
26. Watanabe, T.; Yanagi, H.; Kamiya, T.; Kamihara, Y.; Hiramatsu, H.; Hirano, M.; Hosono, H. Nickel-Based Oxyphosphide Superconductor with a Layered Crystal Structure, LaNiOP. *Inorg. Chem.* **2007**, *46*, 7719–7721. [CrossRef] [PubMed]
27. Gorter, C.J. Superconductivity I. *Physica* **1949**, *15*, 55–64. [CrossRef]
28. Camacho, W.Y.C.; Da Silva, R.M.; Shanenko, A.; Vagov, A.; Vasenko, A.S.; Lvov, B.; Aguiar, J.A.; Cordoba, W.Y. Spontaneous pattern formation in superconducting films. *J. Phys. Condens. Matter* **2019**, *32*, 075403. [CrossRef] [PubMed]
29. Miikkulainen, V.; Leskela, M.; Ritala, M.; Puurunen, R.L. Crystallinity of inorganic films grown by atomic layer deposition: Overview and general trends. *J. Appl. Phys.* **2013**, *113*, 021301. [CrossRef]
30. Hazra, D.; Tsavdaris, N.; Jebari, S.; Grimm, A.; Blanchet, F.; Mercier, F.; Blanquet, E.; Chapelier, C.; Hofheinz, M. Superconducting properties of very high quality NbN thin films grown by high temperature chemical vapor deposition. *Supercond. Sci. Technol.* **2016**, *29*, 105011. [CrossRef]
31. Keskiväli, L.; Putkonen, M.; Puhakka, E.; Kenttä, E.; Kint, J.; Ramachandran, R.K.; Detavernier, C.; Simell, P. Molecular Layer Deposition Using Ring-Opening Reactions: Molecular Modeling of the Film Growth and the Effects of Hydrogen Peroxide. *ACS Omega* **2018**, *3*, 7141–7149. [CrossRef]
32. Hinz, J.; Bauer, A.J.; Frey, L. Analysis of NbN thin film deposition by plasma-enhanced ALD for gate electrode application. *Semicond. Sci. Technol.* **2010**, *25*, 075009. [CrossRef]
33. Ashcroft, N.W.; Mermin, N.D. *Solid State Physics*; Holt, Rinehart and Winston, University of California: Los Angeles, CA, USA, 1976.
34. Ohring, M. *Materials Science of Thin Films: Deposition and Structure*; Academic Press: Cambridge, MA, USA, 2002.
35. Luth, H. *Solid Surfaces, Interfaces and Thin Films*; Springer: New York, NY, USA, 2015.
36. Ruf, J.P.; Paik, H.; Schreiber, N.J.; Nair, H.P.; Miao, L.; Kawasaki, J.K.; Nelson, J.N.; Faeth, B.D.; Lee, Y.; Goodge, B.H.; et al. Strain-stabilized superconductivity. *Nat. Commun.* **2021**, *12*, 59. [CrossRef]
37. Brun, C.; Cren, T.; Roditchev, D. Review of 2D superconductivity: The ultimate case of epitaxial monolayers. *Supercond. Sci. Technol.* **2016**, *30*, 013003. [CrossRef]
38. Fabian, M.D.; Shpiro, B.; Rabani, E.; Neuhauser, D.; Baer, R. Stochastic density functional theory. *WIREs Comput. Mol. Sci.* **2019**, *9*, 1–15. [CrossRef]
39. Klein, O. Theory of Superconductivity. *Nature* **1952**, *169*, 578–579. [CrossRef]
40. Zhou, K.; Wang, J.; Song, Y.; Guo, L.; Guo, J. Highly-Tunable Crystal Structure and Physical Properties in FeSe-Based Superconductors. *Crystal* **2019**, *9*, 560. [CrossRef]
41. Cho, Y.; Kim, S.H.; Kim, B.S.; Kim, Y.; Jeon, W. Modulation of the adsorption chemistry of a precursor in atomic layer deposition to enhance the growth per cycle of a $TiO_2$ thin film. *Phys. Chem. Chem. Phys.* **2021**, *23*, 2568–2574. [CrossRef] [PubMed]
42. Mohlala, L.M.; Jen, T.-C.; Olubambi, P.A. Thermal stability and reactivity of titanium halide precursors for the atomic layer deposition of $TiO_2$ on a Pt (111) surface. *Procedia CIRP* **2020**, *93*, 9–13. [CrossRef]
43. Imai, Y.; Nabeshima, F.; Maeda, A. Comparative Review on Thin Film Growth of Iron-Based Superconductors. *Condens. Matter* **2017**, *2*, 25. [CrossRef]
44. Kamihara, Y.; Watanabe, T.; Hirano, M.; Hosono, H. Iron-Based Layered Superconductor $La[O_{1-x}F_x]FeAs$ (x = 0.05 − 0.12) with Tc = 26 K. *J. Am. Chem. Soc.* **2008**, *130*, 3296–3297. [CrossRef]
45. Iida, K.; Hänisch, J.; Tarantini, C. Fe-based superconducting thin films on metallic substrates: Growth, characteristics, and relevant properties. *Appl. Phys. Rev.* **2018**, *5*, 031304. [CrossRef]
46. Virtanen, P.; Braggio, A.; Giazotto, F. Superconducting size effect in thin films under electric field: Mean-field self-consistent model. *Phys. Rev. B* **2019**, *100*, 224506. [CrossRef]
47. Hiramatsu, H.; Kamiya, T.; Hirano, M.; Hosono, H. Heteroepitaxial film growth of layered compounds with the ZrCuSiAs-type and $ThCr_2Si_2$-type structures: From Cu-based semiconductors to Fe-based superconductors. *Phys. C Supercond.* **2009**, *469*, 657–666. [CrossRef]
48. Hiramatsu, H.; Katase, T.; Kamiya, T.; Hosono, H. Thin Film Growth and Device Fabrication of Iron-Based Superconductors. *J. Phys. Soc. Jpn.* **2012**, *81*, 1–25. [CrossRef]
49. Tanabe, K.; Hosono, H. Frontiers of Research on Iron-Based Superconductors toward Their Application. *Jpn. J. Appl. Phys.* **2011**, *51*, 10005. [CrossRef]
50. Mele, P. Superconducting properties of iron chalcogenide thin films. *Sci. Technol. Adv. Mater.* **2012**, *13*, 054301. [CrossRef] [PubMed]

51. Haindl, S.; Kidszun, M.; Oswald, S.; Hess, C.; Büchner, B.; Kölling, S.; Wilde, L.; Thersleff, T.; Yurchenko, V.V.; Jourdan, M.; et al. Thin film growth of Fe-based superconductors: From fundamental properties to functional devices. A comparative review. *Rep. Prog. Phys.* **2014**, *77*, 046502. [CrossRef]
52. Sadovskii, M.V. High-temperature superconductivity in monolayers FeSe. *Uspekhi Fiz. Nauk* **2016**, *186*, 1035–1057. [CrossRef]
53. Hosono, H.; Yamamoto, A.; Hiramatsu, H.; Ma, Y. Recent advances in iron-based superconductors toward applications. *Mater. Today* **2018**, *21*, 278–302. [CrossRef]
54. Hosono, H.; Tanabe, K.; Takayama-Muromachi, E.; Kageyama, H.; Yamanaka, S.; Kumakura, H.; Nohara, M.; Hiramatsu, H.; Fujitsu, S. Exploration of new superconductors and functional materials, and fabrication of superconducting tapes and wires of iron pnictides. *Sci. Technol. Adv. Mater.* **2015**, *16*, 033503. [CrossRef]
55. Hsu, F.-C.; Luo, J.-Y.; Yeh, K.-W.; Chen, T.-K.; Huang, T.-W.; Wu, P.M.; Lee, Y.-C.; Huang, Y.-L.; Chu, Y.-Y.; Yan, D.-C.; et al. Superconductivity in the PbO-type structure α-FeSe. *Proc. Natl. Acad. Sci. USA* **2008**, *105*, 14262–14264. [CrossRef]
56. Kamihara, Y.; Hiramatsu, H.; Hirano, M.; Kawamura, R.; Yanagi, H.; Kamiya, T.; Hosono, H. Iron-Based Layered Superconductor: LaOFeP. *J. Am. Chem. Soc.* **2006**, *128*, 10012–10013. [CrossRef]
57. Ren, Z.-A.; Che, G.-C.; Dong, X.-L.; Yang, J.; Lu, W.; Yi, W.; Shen, X.-L.; Li, Z.-C.; Sun, L.-L.; Zhou, F.; et al. Superconductivity and phase diagram in iron-based arsenic-oxides ReFeAsO 1−δ (Re = rare-earth metal) without fluorine doping. *Eur. Lett.* **2008**, *83*, 17002. [CrossRef]
58. Kawaguchi, T.; Uemura, H.; Ohno, T.; Watanabe, R.; Tabuchi, M.; Ujihara, T.; Takenaka, K.; Takeda, Y.; Ikuta, H. Epitaxial Growth of NdFeAsO Thin Films by Molecular Beam Epitaxy. *Appl. Phys. Express* **2009**, *2*, 093002. [CrossRef]
59. Kawaguchi, T.; Uemura, H.; Ohno, T.; Tabuchi, M.; Ujihara, T.; Takenaka, K.; Takeda, Y.; Ikuta, H. In situ growth of superconducting NdFeAs(O,F) thin films by molecular beam epitaxy. *Appl. Phys. Lett.* **2010**, *97*, 042509. [CrossRef]
60. Backen, E.; Haindl, S.; Niemeier, T.; Hühne, R.; Freudenberg, T.; Werner, J.; Behr, G.; Schultz, L.; Holzapfel, B. Growth and anisotropy of La(O, F)FeAs thin films deposited by pulsed laser deposition. *Supercond. Sci. Technol.* **2008**, *21*, 122001. [CrossRef]
61. Kidszun, M.; Haindl, S.; Reich, E.; Hänisch, J.; Iida, K.; Schultz, L.; Holzapfel, B. Epitaxial $LaFeAsO_{1-x}F_x$ thin films grown by pulsed laser deposition. *Supercond. Sci. Technol.* **2010**, *23*, 022002. [CrossRef]
62. Ueda, S.; Takeda, S.; Takano, S.; Yamamoto, A.; Naito, M. High-Tc and high-Jc SmFeAs(O,F) films on fluoride substrates grown by molecular beam epitaxy. *Appl. Phys. Lett.* **2011**, *99*, 232505. [CrossRef]
63. Tsukada, I.; Hanawa, M.; Akiike, T.; Nabeshima, F.; Imai, Y.; Ichinose, A.; Komiya, S.; Hikage, T.; Kawaguchi, T.; Ikuta, H.; et al. Epitaxial Growth of FeSe0.5Te0.5Thin Films on CaF2Substrates with High Critical Current Density. *Appl. Phys. Express* **2011**, *4*, 053101. [CrossRef]
64. Haindl, S.; Hanzawa, K.; Sato, H.; Hiramatsu, H.; Hosono, H. In-situ growth of superconducting $SmO_{1-x}F_xFeAs$ thin films by pulsed laser deposition. *Sci. Rep.* **2016**, *6*, 35797. [CrossRef]
65. Kamihara, Y.; Nomura, T.; Hirano, M.; Kim, J.E.; Kato, K.; Takata, M.; Kobayashi, Y.; Kitao, S.; Higashitaniguchi, S.; Yoda, Y.; et al. Electronic and magnetic phase diagram of superconductors, $SmFeAsO_{1-x}F_x$. *New J. Phys.* **2010**, *12*, 1–14. [CrossRef]
66. Rotter, M.; Pangerl, M.; Tegel, M.; Johrendt, D. Superconductivity and Crystal Structures of $(Ba_{1-x}K_x)Fe2As2$(x = 0–1). *Angew. Chem. Int. Ed.* **2008**, *47*, 7949–7952. [CrossRef]
67. Rotter, M.; Tegel, M.; Johrendt, D. Superconductivity at 38 K in the Iron Arsenide$(Ba_{1-x}K_x)Fe_2As_2$. *Phys. Rev. Lett.* **2008**, *101*, 107006. [CrossRef] [PubMed]
68. Lee, N.H.; Jung, S.-G.; Kim, D.H.; Kang, W. Potassium-doped $BaFe_2As_2$ superconducting thin films with a transition temperature of 40 K. *Appl. Phys. Lett.* **2010**, *96*, 202505. [CrossRef]
69. Lee, N.H.; Jung, S.-G.; Ranot, M.; Kang, W. Fabrication details of $Ba_{1-x}K_xFe_2As_2$ films by pulsed laser deposition technique. *Prog. Supercond. Cryog.* **2014**, *16*, 4–6. [CrossRef]
70. Agatsuma, S.; Yamagishi, T.; Takeda, S.; Naito, M. MBE growth of FeSe and $Sr_{1-x}K_xFe_2As_2$. *Phys. C* **2010**, *470*, 1468–1472. [CrossRef]
71. Takeda, S.; Ueda, S.; Yamagishi, T.; Agatsuma, S.; Takano, S.; Mitsuda, A.; Naito, M. Molecular Beam Epitaxy Growth of Superconducting $Sr_{1-x}K_xFe_2As_2$ and $Ba_{1-x}K_xFe_2As_2$. *Appl. Phys. Express* **2010**, *3*, 093101. [CrossRef]
72. Ueda, S.; Yamagishi, T.; Takeda, S.; Agatsuma, S.; Takano, S.; Mitsuda, A.; Naito, M. MBE growth of Fe-based superconducting films. *Phys. C Supercond.* **2011**, *471*, 1167–1173. [CrossRef]
73. Yamagishi, T.; Ueda, S.; Takeda, S.; Takano, S.; Mitsuda, A.; Naito, M. A study of the doping dependence of Tc in $Ba_{1-x}K_xFe_2As_2$ and $Sr_{1-x}K_xFe_2As_2$ films grown by molecular beam epitaxy. *Phys. C Supercond.* **2011**, *471*, 1177–1180. [CrossRef]
74. Wu, M.K.; Hsu, F.C.; Yeh, K.W.; Huang, T.W.; Luo, J.Y.; Wang, M.J.; Chang, H.H.; Chen, T.K.; Rao, S.M.; Mok, B.H.; et al. The development of the superconducting PbO-type β-FeSe and related compounds. *Phys. C* **2009**, *469*, 340–349. [CrossRef]
75. Yeh, K.-W.; Huang, T.-W.; Huang, Y.-L.; Chen, T.-K.; Hsu, F.-C.; Wu, P.M.; Lee, Y.-C.; Chu, Y.-Y.; Chen, C.-L.; Luo, J.-Y.; et al. Tellurium substitution effect on superconductivity of the α-phase iron selenide. *Eur. Lett.* **2008**, *84*, 104502. [CrossRef]
76. Mizuguchi, Y.; Tomioka, F.; Tsuda, S.; Yamaguchi, T.; Takano, Y. Superconductivity at 27K in tetragonal FeSe under high pressure. *Appl. Phys. Lett.* **2008**, *93*, 152505. [CrossRef]
77. Medvedev, S.; McQueen, T.M.; Troyan, I.A.; Palasyuk, T.; Eremets, M.I.; Cava, R.J.; Naghavi, S.; Casper, F.; Ksenofontov, V.; Wortmann, G.; et al. Electronic and magnetic phase diagram of β-Fe1.01Se with superconductivity at 36.7 K under pressure. *Nat. Mater.* **2009**, *8*, 630–633. [CrossRef] [PubMed]

78. Bellingeri, E.; Kawale, S.; Pallecchi, I.; Gerbi, A.; Buzio, R.; Braccini, V.; Palenzona, A.; Putti, M.; Adamo, M.; Sarnelli, E.; et al. Strong vortex pinning in FeSe0.5Te0.5 epitaxial thin film. *Appl. Phys. Lett.* **2012**, *100*, 082601. [CrossRef]
79. Hanzawa, K.; Sato, H.; Hiramatsu, H.; Kamiya, T.; Hosono, H. Electric field-induced superconducting transition of insulating FeSe thin film at 35 K. *Proc. Natl. Acad. Sci. USA* **2016**, *113*, 3986–3990. [CrossRef]
80. Lei, B.; Cui, J.H.; Xiang, Z.J.; Shang, C.; Wang, N.Z.; Ye, G.J.; Luo, X.G.; Wu, T.; Sun, Z.; Chen, X.H. Evolution of High-Temperature Superconductivity from a Low-TcPhase Tuned by Carrier Concentration in FeSe Thin Flakes. *Phys. Rev. Lett.* **2016**, *116*, 077002. [CrossRef] [PubMed]
81. Nabeshima, F.; Imai, Y.; Hanawa, M.; Tsukada, I.; Maeda, A. Enhancement of the superconducting transition temperature in FeSe epitaxial thin films by anisotropic compression. *Appl. Phys. Lett.* **2013**, *103*, 172602. [CrossRef]
82. Wang, Q.-Y.; Li, Z.; Zhang, W.-H.; Zhang, Z.-C.; Zhang, J.-S.; Li, W.; Ding, H.; Ou, Y.-B.; Deng, P.; Chang, K.; et al. Interface-Induced High-Temperature Superconductivity in Single Unit-Cell FeSe Films on $SrTiO_3$. *Chin. Phys. Lett.* **2012**, *29*, 037402. [CrossRef]
83. He, S.; He, J.; Zhang, W.; Zhao, L.; Liu, D.; Liu, X.; Mou, D.; Ou, Y.-B.; Wang, Q.-Y.; Li, Z.; et al. Phase diagram and electronic indication of high-temperature superconductivity at 65 K in single-layer FeSe films. *Nat. Mater.* **2013**, *12*, 605–610. [CrossRef]
84. Ge, J.-F.; Liu, Z.-L.; Liu, C.; Gao, C.-L.; Qian, D.; Xue, Q.-K.; Liu, Y.; Jia, J.-F. Superconductivity above 100 K in single-layer FeSe films on doped $SrTiO_3$. *Nat. Mater.* **2015**, *14*, 285–289. [CrossRef]
85. Putti, M.; Pallecchi, I.; Bellingeri, E.; Cimberle, M.R.; Tropeano, M.; Ferdeghini, C.; Palenzona, A.; Tarantini, C.; Yamamoto, A.; Jiang, J.; et al. New Fe-based superconductors: Properties relevant for applications. *Supercond. Sci. Technol.* **2010**, *23*, 034003. [CrossRef]
86. Imai, Y.; Sawada, Y.; Nabeshima, F.; Maeda, A. Suppression of phase separation and giant enhancement of superconducting transition temperature in $FeSe_{1-x}$ $Te_x$ thin films. *Proc. Natl. Acad. Sci. USA* **2015**, *112*, 1937–1940. [CrossRef]
87. Seo, S.; Kang, J.-H.; Oh, M.J.; Jeong, I.-S.; Jiang, J.; Gu, G.; Lee, J.-W.; Lee, J.; Noh, H.; Liu, M.; et al. Origin of the emergence of higher Tc than bulk in iron chalcogenide thin films. *Sci. Rep.* **2017**, *7*, 1–8. [CrossRef] [PubMed]
88. Hanawa, M.; Ichinose, A.; Komiya, S.; Tsukada, I.; Imai, Y.; Maeda, A. Empirical selection rule of substrate materials for iron chalcogenide superconducting thin films. *Japan. J. Appl. Phys.* **2012**, *51*, 010104. [CrossRef]
89. Iida, K.; Hänisch, J.; Schulze, M.; Aswartham, S.; Wurmehl, S.; Büchner, B.; Schultz, L.; Holzapfel, B. Generic Fe buffer layers for Fe-based superconductors: Epitaxial $FeSe_{1-x}Te_x$ thin films. *Appl. Phys. Lett.* **2011**, *99*, 202503. [CrossRef]
90. Si, W.; Han, S.J.; Shi, X.; Ehrlich, S.N.; Jaroszynski, J.; Goyal, A.; Li, Q. High current superconductivity in FeSe0.5Te0.5-coated conductors at 30 tesla. *Nat. Commun.* **2013**, *4*, 1347. [CrossRef] [PubMed]
91. Ozaki, T.; Wu, L.; Zhang, C.; Jaroszynski, J.; Si, W.; Zhou, J.; Zhu, Y.; Li, Q. A route for a strong increase of critical current in nanostrained iron-based superconductors. *Nat. Commun.* **2016**, *7*, 13036. [CrossRef]
92. Molatta, S.; Haindl, S.; Trommler, S.; Schulze, M.; Wurmehl, S.; Hühne, R. Interface control by homoepitaxial growth in pulsed laser deposited iron chalcogenide thin films. *Sci. Rep.* **2015**, *5*, 16334. [CrossRef]
93. Ozawa, T.C.; Kauzlarich, S.M.; Bieringer, M.; Greedan, J.E. Possible Charge-Density-Wave/Spin-Density-Wave in the Layered Pnictide−Oxides: $Na_2Ti_2Pn_2O$ (Pn = As, Sb). *Chem. Mater.* **2001**, *13*, 1804–1810. [CrossRef]
94. Liu, R.H.; Tan, D.; Song, Y.A.; Li, Q.J.; Yan, Y.J.; Ying, J.J.; Xie, Y.L.; Wang, X.F.; Chen, X.H. Physical properties of the layered pnictide oxides$Na_2Ti_2P_2O$ (P = As,Sb). *Phys. Rev. B* **2009**, *80*, 144516. [CrossRef]
95. Lorenz, B.; Guloy, A.M.; Chu, P.C.W. Superconductivity in titanium-based pnictide oxide compounds. *Int. J. Mod. Phys. B* **2014**, *28*, 1–25. [CrossRef]
96. Yajima, T.; Nakano, K.; Takeiri, F.; Ono, T.; Hosokoshi, Y.; Matsushita, Y.; Hester, J.; Kobayashi, Y.; Kageyama, H. Superconductivity in $BaTi_2Sb_2O$ with ad1Square Lattice. *J. Phys. Soc. Jpn.* **2012**, *81*, 1–4. [CrossRef]
97. Doan, P.; Gooch, M.; Tang, Z.; Lorenz, B.; Möller, A.; Tapp, J.; Chu, P.C.W.; Guloy, A.M. $Ba_{1-x}Na_xTi_2Sb_2O$ ($0.0 \leq x \leq 0.33$): A Layered Titanium-Based Pnictide Oxide Superconductor. *J. Am. Chem. Soc.* **2012**, *134*, 16520–16523. [CrossRef] [PubMed]
98. Yajima, T. Titanium Pnictide Oxide Superconductors. *Condens. Matter* **2017**, *2*, 4. [CrossRef]
99. Adam, A.; Schuster, H.-U. Darstellung und Kristallstruktur der Pnictidoxide $Na_2Ti_2As_2O$ und $Na_2Ti_2Sb_2O$. *ZAAC* **1990**, *584*, 150–158. [CrossRef]
100. Wang, X.; Yan, Y.J.; Ying, J.J.; Li, Q.J.; Zhang, M.; Xu, N.; Chen, X.H. Structure and physical properties for a new layered pnictide-oxide: $BaTi_2As_2O$. *J. Phys. Condens. Matter* **2010**, *22*, 075702. [CrossRef]
101. Yajima, T.; Nakano, K.; Takeiri, F.; Hester, J.; Yamamoto, T.; Kobayashi, Y.; Tsuji, N.; Kim, J.; Fujiwara, A.; Kageyama, H. Synthesis and physical properties of the new oxybismuthides $BaTi_2Bi_2O$ and $(SrF)_2Ti_2Bi_2O$ with a d1 square net. *J. Phys. Soc. Jpn.* **2012**, *82*, 013703. [CrossRef]
102. Liu, R.H.; Song, Y.A.; Li, Q.J.; Ying, J.J.; Yan, Y.J.; He, Y.; Chen, X. Structure and Physical Properties of the Layered Pnictide-Oxides: $(SrF)_2Ti_2Pn_2O$ (Pn= As, Sb) and $(SmO)_2Ti_2Sb_2O$. *Chem. Mater.* **2010**, *22*, 1503–1508. [CrossRef]
103. Singh, D.J. Electronic structure, disconnected Fermi surfaces and antiferromagnetism in the layered pnictide superconductor $NaxBa_{1-x}Ti_2Sb_2O$. *New J. Phys.* **2012**, *14*, 123003. [CrossRef]
104. Suetin, D.V.; Ivanovskii, A.L. Electronic properties and fermi surface for new Fe-free layered pnictide-oxide superconductor $BaTi_2Bi_2O$ from first principles. *JETP Lett.* **2013**, *97*, 220–225. [CrossRef]
105. Bussmann-Holder, A.; Keller, H. High-temperature superconductors: Underlying physics and applications. *Z. Für Nat. B* **2020**, *75*, 3–14. [CrossRef]
106. Müller, K.A.; Kool, T.W. Superconductivity. *Prop. Perovskites Other Oxides* **2010**, *193*, 545–562. [CrossRef]

107. Mine, T.; Yanagi, H.; Kamiya, T.; Kamihara, Y.; Hirano, M.; Hosono, H. Nickel-based phosphide superconductor with infinite-layer structure, BaNi2P2. *Solid State Commun.* **2008**, *147*, 111–113. [CrossRef]
108. Laloë, J.-B.; Kim, T.H.; Moodera, J.S. Molecular-Beam Epitaxially Grown $MgB_2$Thin Films and Superconducting Tunnel Junctions. *Adv. Condens. Matter Phys.* **2011**, *2011*, 989732. [CrossRef]
109. Askerzade, I. The upper critical field of thin films of two-band superconductors: An application to $MgB_2$. *Mod. Phys. Lett. B* **2004**, *18*, 1525–1531. [CrossRef]
110. Yamanaka, S.; Enishi, E.; Fukuoka, H.; Yasukawa, M. High-Pressure Synthesis of a New Silicon Clathrate Superconductor, Ba8Si46. *Inorg. Chem.* **2000**, *39*, 56–58. [CrossRef]
111. Yamanaka, S. Intercalation and superconductivity in ternary layer structured metal nitride halides (MNX: M = Ti, Zr, Hf; X = Cl, Br, I). *J. Mater. Chem.* **2010**, *20*, 2922–2933. [CrossRef]
112. Yamanaka, S.; Okumura, H.; Zhu, L. Alkali metal intercalation in layer structured α-HfNBr☆. *J. Phys. Chem. Solids* **2004**, *65*, 565–569. [CrossRef]
113. Kuroki, K. Spin-fluctuation-mediatedd+id′pairing mechanism in dopedβ-MNCl(M = Hf,Zr)superconductors. *Phys. Rev. B* **2010**, *81*, 1–7. [CrossRef]
114. Bill, A.; Morawitz, H.; Kresin, V.Z. Dynamical screening and superconducting state in intercalated layered metallochloronitrides. *Phys. Rev. B* **2002**, *66*, 100501. [CrossRef]
115. Bill, A.; Morawitz, H.; Kresin, V.Z. Electronic collective modes and superconductivity in layered conductors. *Phys. Rev. B* **2003**, *68*, 144519. [CrossRef]
116. Yamanaka, S.; Hotehama, K.-I.; Kawaji, H. Superconductivity at 25.5 K in electron-doped layered hafnium nitride. *Nature* **1998**, *392*, 580–582. [CrossRef]
117. Yamanaka, S.; Kawaji, H.; Hotehama, K.-I.; Ohashi, M. A new layer-structured nitride superconductor. Lithium-intercalatedβ-zirconium nitride chloride, LixZrNCl. *Adv. Mater.* **1996**, *8*, 771–774. [CrossRef]
118. Yamanaka, S.; Izumi, S.; Maekawa, S.; Umemoto, K. Phase diagram of the La–Si binary system under high pressure and the structures of superconducting $LaSi_5$ and $LaSi_{10}$. *J. Solid State Chem.* **2009**, *182*, 1991–2003. [CrossRef]
119. Yamanaka, S.; Maekawa, S. Structural Evolution of the Binary System Ba-Si under High-pressure and High-temperature Conditions. *Z. Für Nat. B* **2006**, *61*, 1493–1499. [CrossRef]
120. Kurakevych, O.O.; Strobel, T.A.; Kim, D.Y.; Muramatsu, T.; Struzhkin, V.V. Na-Si Clathrates Are High-Pressure Phases: A Melt-Based Route to Control Stoichiometry and Properties. *Cryst. Growth Des.* **2013**, *13*, 303–307. [CrossRef]
121. Zhang, S.; Tanaka, M.; Watanabe, E.; Zhu, H.; Inumaru, K.; Yamanaka, S. Superconductivity of alkali metal intercalated TiNBr with α-type nitride layers. *Supercond. Sci. Technol.* **2013**, *26*, 122001. [CrossRef]
122. Ronning, F.; Bauer, E.D.; Park, T.; Baek, S.-H.; Sakai, H.; Thompson, J.D. Superconductivity and the effects of pressure and structure in single-crystalline$SrNi_2P_2$. *Phys. Rev. B* **2009**, *79*, 134507. [CrossRef]
123. Hirai, D.; Takayama, T.; Higashinaka, R.; Aruga-Katori, H.; Takagi, H. Superconductivity in Layered Pnictides $BaRh_2P_2$ and $BaIr_2P_2$. *J. Phys. Soc. Jpn.* **2009**, *78*, 1–4. [CrossRef]
124. Jeitschko, W.; Glaum, R.; Boonk, L. Superconducting $LaRu_2P_2$ and other alkaline earth and rare earth metal ruthenium and osmium phosphides and arsenides with $ThCr_2Si_2$ structure. *J. Solid State Chem.* **1987**, *69*, 93–100. [CrossRef]
125. Han, J.-T.; Zhou, J.-S.; Cheng, J.-G.; Goodenough, J.B. A New Pnictide Superconductor without Iron. *J. Am. Chem. Soc.* **2009**, *132*, 908–909. [CrossRef]
126. Bauer, E.; Ronning, F.; Scott, B.; Thompson, J.D. Superconductivity in$SrNi_2As_2$single crystals. *Phys. Rev. B* **2008**, *78*, 172504. [CrossRef]
127. Ronning, F.; Kurita, N.; Bauer, E.; Scott, B.; Park, T.; Klimczuk, T.; Movshovich, R.; Thompson, J.D. The first order phase transition and superconductivity in $BaNi_2As_2$single crystals. *J. Phys. Condens. Matter* **2008**, *20*, 342203. [CrossRef]
128. Imre, A.; Hellmann, A.; Wenski, G.; Graf, J.; Johrendt, D.; Mewis, A. Inkommensurabel modulierte Kristallstrukturen und Phasenumwandlungen–Die Verbindungen $SrPt_2As_2$ und $EuPt_2As_2$. *Z. Für Anorg. Und Allg. Chem.* **2007**, *633*, 2037–2045. [CrossRef]
129. Tsutsumi, K.; Takayanagi, S.; Ishikawa, M.; Hirano, T. Superconductivity of Intermetallic Compound $CoSi_2$. *J. Phys. Soc. Jpn.* **1995**, *64*, 2237. [CrossRef]
130. Sefat, A.; McGuire, M.; Jin, R.; Sales, B.C.; Mandrus, D.; Ronning, F.; Bauer, E.; Mozharivskyj, Y. Structure and anisotropic properties of$BaFe_2$-x$NixAs_2$(x = 0, 1, and 2) single crystals. *Phys. Rev. B* **2009**, *79*, 094508. [CrossRef]
131. Kurita, N.; Ronning, F.; Tokiwa, Y.; Bauer, E.D.; Subedi, A.; Singh, D.J.; Thompson, J.D.; Movshovich, R. Low-Temperature Magnetothermal Transport Investigation of a Ni-Based Superconductor$BaNi_2As_2$: Evidence for Fully Gapped Superconductivity. *Phys. Rev. Lett.* **2009**, *102*, 147004. [CrossRef]
132. Subedi, A.; Singh, D.J. Density functional study of$BaNi_2As_2$: Electronic structure, phonons, and electron-phonon superconductivity. *Phys. Rev. B* **2008**, *78*, 132511. [CrossRef]
133. Shein, I.R.; Ivanovskii, A.L. Electronic and structural properties of low-temperature superconductors and ternary pnictides $ANi_2Pn_2$ (A = Sr, BaandPn = P,As). *Phys. Rev. B* **2009**, *79*, 054510. [CrossRef]
134. Kudo, K.; Takasuga, M.; Okamoto, Y.; Hiroi, Z.; Nohara, M. Giant Phonon Softening and Enhancement of Superconductivity by Phosphorus Doping of$BaNi_2As_2$. *Phys. Rev. Lett.* **2012**, *109*, 097002. [CrossRef]

135. Toriyama, T.; Kobori, M.; Konishi, T.; Ohta, Y.; Sugimoto, K.; Kim, J.; Fujiwara, A.; Pyon, S.; Kudo, K.; Nohara, M. Switching of Conducting Planes by Partial Dimer Formation in $IrTe_2$. *J. Phys. Soc. Jpn.* **2014**, *83*, 33701. [CrossRef]
136. Pyon, S.; Kudo, K.; Nohara, M. Emergence of superconductivity near the structural phase boundary in Pt-doped $IrTe_2$ single crystals. *Physica C.* **2013**, *494*, 80–84. [CrossRef]
137. Joseph, B.; Bendele, M.; Simonelli, L.; Maugeri, L.; Pyon, S.; Kudo, K. Local structural displacements across the structural phase transition in $IrTe_2$: Order-disorder of dimers and role of Ir-Te correlations. *Phys Rev B.* **2013**, *88*, 3–6. [CrossRef]
138. Jobic, S.; Evain, M.; Brec, R.; Deniard, P.; Jouanneaux, A.; Rouxel, J. Crystal structure of polymeric pyrite type $Ir_2Te_2$. *J. Solid State Chem.* **1991**, *95*, 319–326. [CrossRef]
139. Léger, J.; Pereira, A.; Haines, J.; Jobic, S.; Brec, R. Phase transformations of polymeric $CdI_2$-type $IrTe_2$ under high pressure. *J. Phys. Chem. Solids* **2000**, *61*, 27–34. [CrossRef]
140. Qi, Y.; Matsuishi, S.; Guo, J.; Mizoguchi, H.; Hosono, H. Superconductivity in Defective Pyrite-Type Iridium ChalcogenidesIrx-$Ch_2$(Ch = Seand Te). *Phys. Rev. Lett.* **2012**, *109*, 217002. [CrossRef] [PubMed]
141. Gor'Kov, L.P.; Rashba, E.I. Superconducting 2D System with Lifted Spin Degeneracy: Mixed Singlet-Triplet State. *Phys. Rev. Lett.* **2001**, *87*, 037004. [CrossRef]
142. Frigeri, P.A.; Agterberg, D.F.; Sigrist, M. Spin susceptibility in superconductors without inversion symmetry. *New J. Phys.* **2004**, *6*, 115. [CrossRef]
143. Frigeri, P.A.; Agterberg, D.F.; Koga, A.; Sigrist, M. Superconductivity without Inversion Symmetry: MnSi versusCePt3Si. *Phys. Rev. Lett.* **2004**, *92*, 097001. [CrossRef]
144. Bauer, E.D.; Hilscher, G.; Michor, H.; Paul, C.; Scheidt, E.W.; Gribanov, A.V.; Seropegin, Y.; Noël, H.; Sigrist, M.; Rogl, P. Heavy Fermion Superconductivity and Magnetic Order in NoncentrosymmetricCePt3Si. *Phys. Rev. Lett.* **2004**, *92*, 027003. [CrossRef]
145. Settai, R.; Sugitani, I.; Okuda, Y.; Thamizhavel, A.; Nakashima, M.; Ōnuki, Y.; Harima, H. Pressure-induced superconductivity in $CeCoGe_3$ without inversion symmetry. *J. Magn. Magn. Mater.* **2007**, *310*, 844–846. [CrossRef]
146. Kimura, N.; Ito, K.; Aoki, H.; Uji, S.; Terashima, T. Extremely High Upper Critical Magnetic Field of the Noncentrosymmetric Heavy Fermion SuperconductorCeRhSi$_3$. *Phys. Rev. Lett.* **2007**, *98*, 197001. [CrossRef]
147. Isobe, M.; Yoshida, H.; Kimoto, K.; Arai, M.; Takayama-Muromachi, E. SrAuSi$_3$: A Noncentrosymmetric Superconductor. *Cheminform* **2014**, *26*, 2155–2165. [CrossRef]
148. Pyon, S.; Kudo, K.; Matsumura, J.-I.; Ishii, H.; Matsuo, G.; Nohara, M.; Hojo, H.; Oka, K.; Azuma, M.; Garlea, V.O.; et al. Superconductivity in Noncentrosymmetric Iridium Silicide $Li_2IrSi_3$. *J. Phys. Soc. Jpn.* **2014**, *83*, 1–5. [CrossRef]
149. McMillan, W.L. Transition Temperature of Strong-Coupled Superconductors. *Phys. Rev.* **1968**, *167*, 331–344. [CrossRef]
150. Dynes, R. McMillan's equation and the Tc of superconductors. *Solid State Commun.* **1972**, *10*, 615–618. [CrossRef]
151. Zheng, X.; Zheng, J. Seeking high temperature superconductors in ambient from exemplary beryllium-based alloys. *Solid State Commun.* **2019**, *306*, 113769. [CrossRef]
152. Ryu, G.; Kim, S.W.; Mizoguchi, H.; Matsuishi, S.; Hosono, H. Superconductivity in a PbFCl-type pnictide: NbSiAs. *Eur. Lett.* **2012**, *99*, 27002. [CrossRef]
153. Mizoguchi, H.; Hosono, H. $La_2Sb$, a layered superconductor with metal–metal bonds. *Chem. Commun.* **2011**, *47*, 3778–3780. [CrossRef] [PubMed]
154. Guo, J.; Yamaura, J.-I.; Lei, H.; Matsuishi, S.; Qi, Y.; Hosono, H. Superconductivity in Ban+2Ir4nGe12n+4(n = 1,2) with cage structure and softening of low-lying localized mode. *Phys. Rev. B* **2013**, *88*, 1–5. [CrossRef]
155. Ryu, G.; Kim, S.W.; Matsuishi, S.; Kawaji, H.; Hosono, H. Superconductivity in Nb4MSi (M = Ni, Co, and Fe) with a quasi-two-dimensional Nb network. *Phys. Rev. B* **2011**, *84*, 1–6. [CrossRef]
156. Li, Y.; Weng, Y.; Zhang, J.; Ding, J.; Zhu, Y.; Wang, Q.; Yang, Y.; Cheng, Y.; Zhang, Q.; Li, P.; et al. Observation of superconductivity in structure-selected $Ti_2O_3$ thin films. *NPG Asia Mater.* **2018**, *10*, 522–532. [CrossRef]
157. Jeong, S.; Matsuishi, S.; Lee, K.; Toda, Y.; Kim, S.W.; Hosono, H. Superconductivity of Ca2InN with a layered structure embedding an anionic indium chain array. *Arxiv Prepr.* **2014**, arXiv:1403.1348.
158. Arpaia, R.; Golubev, D.; Baghdadi, R.; Ciancio, R.; Dražić, G.; Orgiani, P.; Montemurro, D.; Bauch, T.; Lombardi, F. Transport properties of ultrathin $YBa_2Cu_3O_{7-\delta}$ nanowires: A route to single-photon detection. *Phys. Rev. B* **2017**, *96*, 064525. [CrossRef]
159. Stepantsov, E.A.; Arpaia, R.; Lombardi, F. Growth of twin-free b-oriented $YBa_2Cu_3O_7$ − x films. *Crystallogr. Rep.* **2015**, *60*, 393–396. [CrossRef]
160. Stepantsov, E.A.; Lombardi, F.; Winkler, D. Growth of $YBa_2Cu_3O_7$ films with [100] tilt of CuO planes to the surface on $SrTiO_3$ crystals. *Crystallogr. Rep.* **2011**, *56*, 152–156. [CrossRef]
161. Kislinskii, J.; Zhao, B.-R.; Wu, P.-J.; Peng, Z.-Q.; Chen, Y.-F.; Yang, T.; Chen, L.; Sun, J.-J.; Xu, B.; Wu, F.; et al. $YBa_2Cu_3O_7$ Bicrystal Josephson Junctions and dc SQUIDs. *Chin. Phys. Lett.* **1996**, *13*, 390–393. [CrossRef]
162. Carillo, F.; De Luca, G.M.; Montemurro, D.; Papari, G.P.; Salluzzo, M.; Stornaiuolo, D.; Tafuri, F.; Beltram, F. Coherent transport in extremely underdoped Nd1.2Ba1.8Cu3Oznanostructures. *New J. Phys.* **2012**, *14*, 1–10. [CrossRef]
163. Chaix, L.; Ghiringhelli, G.; Peng, Y.; Hashimoto, M.; Moritz, B.; Kummer, K.; Brookes, N.; He, Y.; Chen, S.; Ishida, S.; et al. Dispersive charge density wave excitations in $Bi_2Sr_2CaCu_2O_{8+\delta}$. *Nat. Phys.* **2017**, *13*, 952–956. [CrossRef]
164. Shayesteh, P.; Tsyshevsky, R.; Urpelainen, S.; Rochet, F.; Bournel, F.; Gallet, J.-J.; Kuklja, M.M.; Schnadt, J.; Head, A.R. Experimental and theoretical gas phase electronic structure study of tetrakis(dimethylamino) complexes of Ti(IV) and Hf(IV). *J. Electron Spectrosc. Relat. Phenom.* **2019**, *234*, 80–85. [CrossRef]

165. Burdastyh, M.V.; Postolova, S.V.; Proslier, T.; Ustavshikov, S.S.; Antonov, A.V.; Vinokur, V.M.; Mironov, A.Y. Superconducting phase transitions in disordered NbTiN films. *Sci. Rep.* **2020**, *10*, 1–7. [CrossRef]
166. Janocha, E.; Pettenkofer, C. ALD of ZnO using diethylzinc as metal-precursor and oxygen as oxidizing agent. *Appl. Surf. Sci.* **2011**, *257*, 10031–10035. [CrossRef]
167. Acharya, J.; Goul, R.; Romine, D.; Sakidja, R.; Wu, J. Effect of $Al_2O_3$ Seed-Layer on the Dielectric and Electrical Properties of Ultrathin MgO Films Fabricated Using In Situ Atomic Layer Deposition. *ACS Appl. Mater. Interfaces* **2019**, *11*, 30368–30375. [CrossRef] [PubMed]
168. Weimer, A.W. Particle atomic layer deposition. *J. Nanoparticle Res.* **2019**, *21*, 1–42. [CrossRef] [PubMed]
169. Van Toan, N.; Tuoi, T.T.K.; Inomata, N.; Toda, M.; Ono, T. Aluminum doped zinc oxide deposited by atomic layer deposition and its applications to micro/nano devices. *Sci. Rep.* **2021**, *11*, 1204. [CrossRef]
170. Shibalov, M.V.; Mumlyakov, A.; Trofimov, I.; Timofeeva, E.; Sirotina, A.; Pershina, E.; Tagachenkov, A.; Anufriev, Y.; Zenova, E.; Porokhov, N.N.; et al. Multistep atomic layer deposition process for ultrathin superconducting NbN films with high critical current density on amorphous substrate. *Supercond. Sci. Technol.* **2021**, *34*, 085016. [CrossRef]
171. Guerrero-Sanchez, J.; Chen, B.; Takeuchi, N.; Zaera, F. Role of oligomer structures in the surface chemistry of amidinate metal complexes used for atomic layer deposition of thin films. *J. Mater. Res.* **2019**, *35*, 720–731. [CrossRef]
172. George, S.M. Atomic Layer Deposition: An Overview. *Chem. Rev.* **2009**, *110*, 111–131. [CrossRef]
173. Tsai, F.-T.; Chao, C.-K.; Jhong, K.-J.; Chang, R.-C. Characterization of oxide barrier layers prepared by atomic layer deposition. *Adv. Mech. Eng.* **2017**, *9*, 1–7. [CrossRef]
174. Oviroh, P.O.; Akbarzadeh, R.; Pan, D.; Coetzee, R.A.M.; Jen, T.-C. New development of atomic layer deposition: Processes, methods and applications. *Sci. Technol. Adv. Mater.* **2019**, *20*, 465–496. [CrossRef]
175. Becker, M.; Sierka, M. Atomistic Simulations of Plasma-Enhanced Atomic Layer Deposition. *Materials* **2019**, *12*, 2605. [CrossRef]
176. Seweryn, A.; Pielok, A.; Lawniczak-Jablonska, K.; Pietruszka, R.; Marcinkowska, K.; Sikora, M.; Witkowski, B.S.; Godlewski, M.; Marycz, K. Zirconium Oxide Thin Films Obtained by Atomic Layer Deposition Technology Abolish the Anti-Osteogenic Effect Resulting from miR-21 Inhibition in the Pre-Osteoblastic $MC_3T_3$ Cell Line. *Int. J. Nanomed.* **2020**, *15*, 1595–1610. [CrossRef]
177. Tvarog, D.; Olejníček, J.; Kratochvíl, J.; Kšírová, P.; Poruba, A.; Hubička, Z.; Čada, M. Characterization of radical-enhanced atomic layer deposition process based on microwave surface wave generated plasma. *J. Appl. Phys.* **2021**, *130*, 013301. [CrossRef]
178. Guo, Y.; Zou, Y.; Cheng, C.; Wang, L.; Made, R.I.; Goei, R.; Tan, K.W.; Li, S.; Tok, A.I.Y. Noble metal alloy thin films by atomic layer deposition and rapid Joule heating. *Sci. Rep.* **2022**, *12*, 1–9. [CrossRef] [PubMed]
179. Sheng, J.; Lee, J.-H.; Choi, W.-H.; Hong, T.; Kim, M.; Park, J.-S. Review Article: Atomic layer deposition for oxide semiconductor thin film transistors: Advances in research and development. *J. Vac. Sci. Technol. A: Vac. Surf. Film.* **2018**, *36*, 060801. [CrossRef]
180. Richey, N.E.; De Paula, C.; Bent, S.F. Understanding chemical and physical mechanisms in atomic layer deposition. *J. Chem. Phys.* **2020**, *152*, 040902. [CrossRef] [PubMed]
181. Sowa, M.J.; Yemane, Y.; Zhang, J.; Palmstrom, J.C.; Ju, L.; Strandwitz, N.C.; Prinz, F.B.; Provine, J. Plasma-enhanced atomic layer deposition of superconducting niobium nitride. *J. Vac. Sci. Technol. A Vac. Surf. Film.* **2017**, *35*, 01B143. [CrossRef]
182. Yemane, Y.T.; Sowa, M.J.; Zhang, J.; Ju, L.; Deguns, E.W.; Strandwitz, N.C.; Prinz, F.B.; Provine, J. Superconducting niobium titanium nitride thin films deposited by plasma-enhanced atomic layer deposition. *Supercond. Sci. Technol.* **2017**, *30*, 095010. [CrossRef]
183. Zhang, K.; Balasubramanian, K.; Ozsdolay, B.; Mulligan, C.; Khare, S.; Zheng, W.; Gall, D. Growth and mechanical properties of epitaxial NbN(001) films on MgO(001). *Surf. Coat. Technol.* **2016**, *288*, 105–114. [CrossRef]
184. Krishnan, R.; David, C.; Ajikumar, P.; Dash, S.; Tyagi, A.; Jayaram, V.; Raj, B. Reactive pulsed laser deposition and characterization of niobium nitride thin films. *Surf. Coat. Technol.* **2011**, *206*, 1196–1202. [CrossRef]
185. Mamun, A.; Farha, A.; Er, A.; Ufuktepe, Y.; Gu, D.; Elsayed-Ali, H.; Elmustafa, A. Nanomechanical properties of NbN films prepared by pulsed laser deposition using nanoindendation. *Appl. Surf. Sci.* **2012**, *258*, 4308–4313. [CrossRef]
186. Hinz, J.; Bauer, A.J.; Thiede, T.; Fischer, R.A.; Frey, L. Evaluation of NbN thin films grown by MOCVD and plasma-enhanced ALD for gate electrode application in high-k/$SiO_2$gate stacks. *Semicond. Sci. Technol.* **2010**, *25*, 075009. [CrossRef]
187. Van Hoornick, N.; De Witte, H.; Witters, T.; Zhao, C.; Conard, T.; Huotari, H.; Swerts, J.; Schram, T.; Maes, J.W.; De Gendt, S.; et al. Evaluation of Atomic Layer Deposited NbN and NbSiN as Metal Gate Materials. *J. Electrochem. Soc.* **2006**, *153*, G437–G442. [CrossRef]
188. Thiede, T.B.; Parala, H.; Reuter, K.; Passing, G.; Kirchmeyer, S.; Hinz, J.; Lemberger, M.; Bauer, A.J.; Barreca, D.; Gasparotto, A.; et al. Deposition of Niobium Nitride Thin Films fromTert-Butylamido-Tris-(Diethylamido)-Niobium by a Modified Industrial MOCVD Reactor. *Chem. Vap. Depos.* **2009**, *15*, 334–341. [CrossRef]
189. Gordon, R.G.; Liu, X.; Shi, Y. Highly conformal diffusion barriers of amorphous niobium nitride. *Mat. Res. Soc. Symp. Proc.* **1999**, *564*, 335–340. [CrossRef]
190. Alén, P.; Ritala, M.; Arstila, K.; Keinonen, J.; Leskelä, M. The growth and diffusion barrier properties of atomic layer deposited NbNx thin films. *Thin Solid Film.* **2005**, *491*, 235–241. [CrossRef]
191. Ziegler, M.; Fritzsch, L.; Day, J.; Linzen, S.; Anders, S.; Toussaint, J.; Meyer, H.-G. Superconducting niobium nitride thin films deposited by metal organic plasma-enhanced atomic layer deposition. *Supercond. Sci. Technol.* **2012**, *26*, 25008. [CrossRef]
192. Chaudhuri, S.; Nevala, M.R.; Maasilta, I.J. Niobium nitride-based normal metal-insulator-superconductor tunnel junction microthermometer. *Appl. Phys. Lett.* **2013**, *102*, 132601. [CrossRef]

193. Hiltunen, L.; Leskela, M.; Mäkelä, M.; Niinistö, L.; Nykänen, E.; Soininen, P. Nitrides of titanium, niobium, tantalum and molybdenum grown as thin films by the atomic layer epitaxy method. *Thin Solid Film.* **1988**, *166*, 149–154. [CrossRef]
194. Klug, J.A.; Proslier, T.; Elam, J.W.; Cook, R.E.; Hiller, J.M.; Claus, H.; Becker, N.G.; Pellin, M.J. Atomic Layer Deposition of Amorphous Niobium Carbide-Based Thin Film Superconductors. *J. Phys. Chem. C* **2011**, *115*, 25063–25071. [CrossRef]
195. Iosad, N.; Roddatis, V.; Polyakov, S.; Varlashkin, A.; Jackson, B.; Dmitriev, P.; Gao, J.; Klapwijk, T. Superconducting transition metal nitride films for THz SIS mixers. *IEEE Trans. Appl. Supercond.* **2001**, *11*, 3832–3835. [CrossRef]
196. Krause, S.; Meledin, D.; Desmaris, V.; Pavolotsky, A.; Belitsky, V.; Rudziński, M.; Pippel, E. Epitaxial growth of ultra-thin NbN films on AlxGa$_{1-x}$N buffer-layers. *Supercond. Sci. Technol.* **2014**, *27*, 65009. [CrossRef]
197. Shiino, T.; Shiba, S.; Sakai, N.; Yamakura, T.; Jiang, L.; Uzawa, Y.; Maezawa, H.; Yamamoto, S. Improvement of the critical temperature of superconducting NbTiN and NbN thin films using the AlN buffer layer. *Supercond. Sci. Technol.* **2010**, *23*, 045004. [CrossRef]
198. Shoji, A.; Kiryu, S.; Kohjiro, S. Superconducting properties and normal-state resistivity of single-crystal NbN films prepared by a reactive rf-magnetron sputtering method. *Appl. Phys. Lett.* **1992**, *60*, 1624–1626. [CrossRef]
199. Wang, Z.; Kawakami, A.; Uzawa, Y.; Komiyama, B. Superconducting properties and crystal structures of single-crystal niobium nitride thin films deposited at ambient substrate temperature. *J. Appl. Phys.* **1996**, *79*, 7837–7842. [CrossRef]
200. Bhat, A.; Meng, X.; Wong, A.; Van Duzer, T. Superconducting NbN films grown using pulsed laser deposition for potential application in internally shunted Josephson junctions. *Supercond. Sci. Technol.* **1999**, *12*, 1030–1032. [CrossRef]
201. Tamm, A.; Tarre, A.; Verchenko, V.; Seemen, H.; Stern, R. Atomic Layer Deposition of Superconducting CuO Thin Films on Three-Dimensional Substrates. *Crystals* **2020**, *10*, 650. [CrossRef]
202. Wei, X.; Roy, P.; Yang, Z.; Zhang, D.; He, Z.; Lu, P.; Licata, O.; Wang, H.; Mazumder, B.; Patibandla, N.; et al. Ultrathin epitaxial NbN superconducting films with high upper critical field grown at low temperature. *Mater. Res. Lett.* **2021**, *9*, 336–342. [CrossRef]
203. Gerbershagen, A.; Calzolaio, C.; Meer, D.; Sanfilippo, S.; Schippers, M. The advantages and challenges of superconducting magnets in particle therapy. *Supercond. Sci. Technol.* **2016**, *29*, 083001. [CrossRef]
204. Jones, D.G.C. "Large Hadron Collider". Encyclopedia Britannica, 22 December 2021. Available online: https://www.britannica.com/technology/Large-Hadron-Collider (accessed on 17 March 2022).
205. Narlikar, A. *The Oxford Handbook of Small Superconductors*, 1st ed.; Oxford University Press: New York, NY, USA, 2017.
206. Luiz, A. Overview of Possible Applications of High Tc Superconductors. In *Applications of High-Tc Superconductivity*; Federal University of Rio de Janeiro: Rio de Janeiro, Brazil, 2011; pp. 2–16.
207. Norton, D.P. Science and technology of high-temperature superconducting films. *Annu. Rev. Mater. Sci.* **1998**, *28*, 299–347. [CrossRef]
208. Sarker, M.M.; Flavell, W. Review of Applications of High-Temperature Superconductors. *J. Supercond.* **1998**, *11*, 209–213. [CrossRef]
209. Parizh, M.; Lvovsky, Y.; Sumption, M. Conductors for commercial MRI magnets beyond NbTi: Requirements and challenges. *Supercond. Sci. Technol.* **2016**, *30*, 014007. [CrossRef]
210. Lee, G.-J. Superconductivity Application in Power System. In *Applications of High-Tc Superconductivity*; Luiz, A., Ed.; Federal University of Rio de Janeiro: Rio de Janeiro, Brazil, 2011; pp. 46–66.
211. Hawsey, R.A.; Morozumi, S. The Energy and Environmental Benefits of Superconducting Power Products. *Mitig. Adapt. Strat. Glob. Chang.* **2005**, *10*, 279–306. [CrossRef]
212. Pereira, V.; Kunkolienkar, G.R. EMP (Electro-Magnetic Pulse) weapon technology along with EMP shielding & detection methodology. In Proceedings of the 2013 Fourth International Conference on Computing, Communications and Networking Technologies (ICCCNT), Tiruchengode, India, 4–6 July 2013; pp. 1–5. [CrossRef]
213. Tou, H.; Tanaka, Y.J.; Sera, M.; Taguchi, Y.; Sasaki, T.; Iwasa, Y.; Zhu, L.; Yamanaka, S. Upper critical field in the electron-doped layered superconductorZrNCl0.7: Magnetoresistance studies. *Phys. Rev. B* **2005**, *72*, 020501. [CrossRef]
214. Sugimoto, A.; Shohara, K.; Ekino, T.; Zheng, Z.; Yamanaka, S. Nanoscale electronic structure of the layered nitride superconductorsα-KxTiNCl andβ-HfNClyobserved by scanning tunneling microscopy and spectroscopy. *Phys. Rev. B* **2012**, *85*. [CrossRef]
215. Grant, P.M. Challenges Confronting High Temperature Superconducting Materials: From Nanoscale Theories to Exascale Energy Applications. *MRS Proc.* **2014**, *1684*, 1–9. [CrossRef]